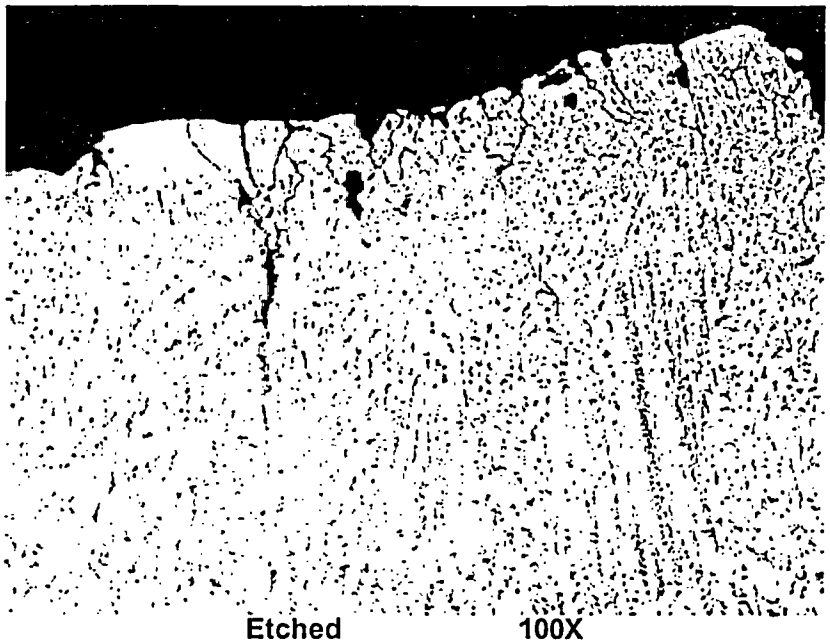

Etched 100X

Etched 375X

Figure 6.1.1.2: Micrographs showing intergranular attack (IGA) and intergranular or interdendritic cracking on the exposed stainless steel cladding.

As-polished 48X

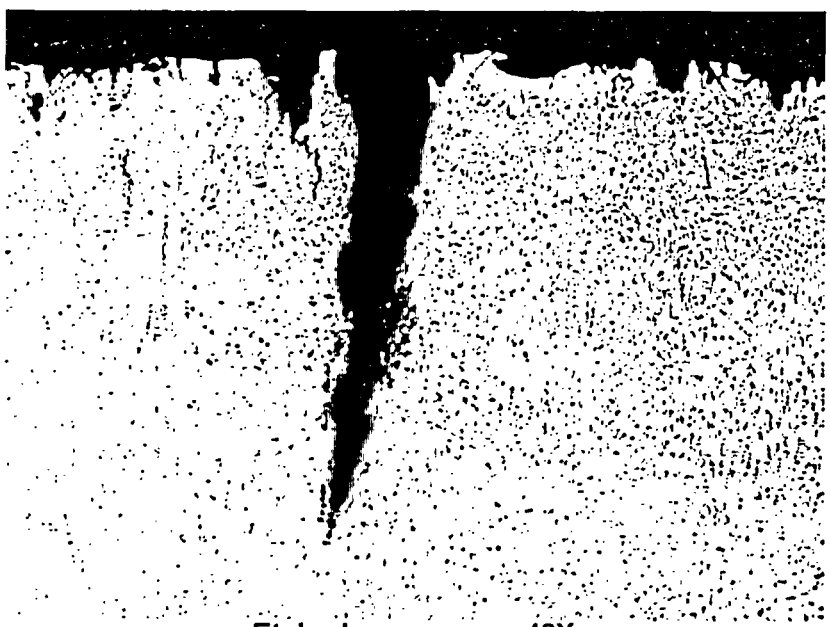

Etched 48X

Figure 6.1.1.3: Micrographs showing the deepest crack observed in A2A7M. Fine intergranular or interdendritic cracks emanating from the crack tip are visible. The crack tip is estimated to be approximately 0.057" (1.47 mm) below the surface. The cracks in the above two photos are the same, but are shown at slightly different planes due to re-polishing.

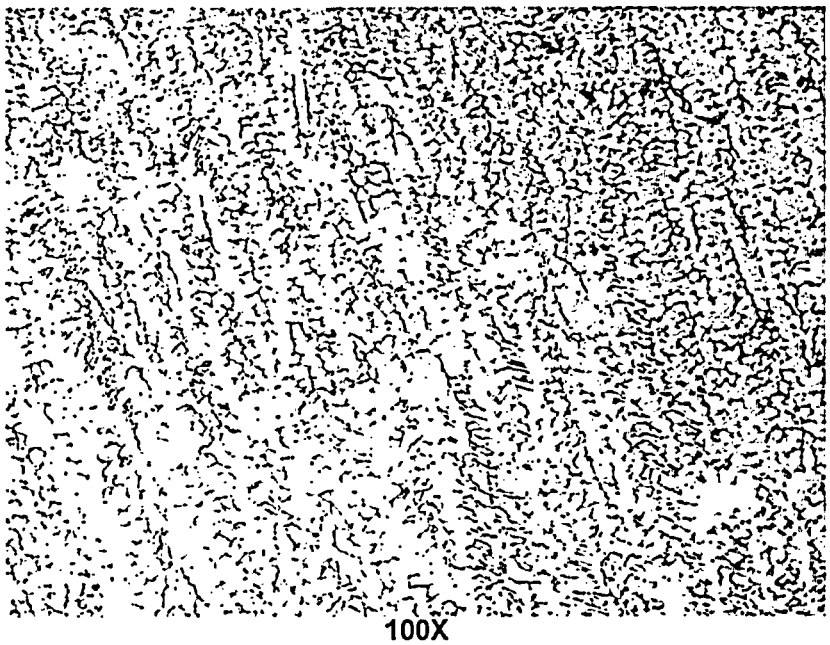

100X

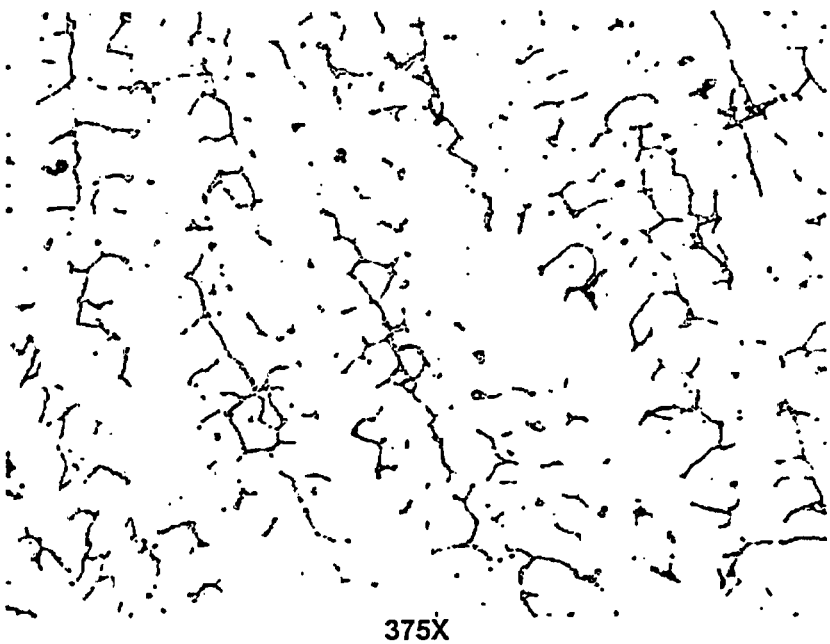

375X

Figure 6.1.1.4: Typical clad microstructure in the mid-thickness of the cladding.

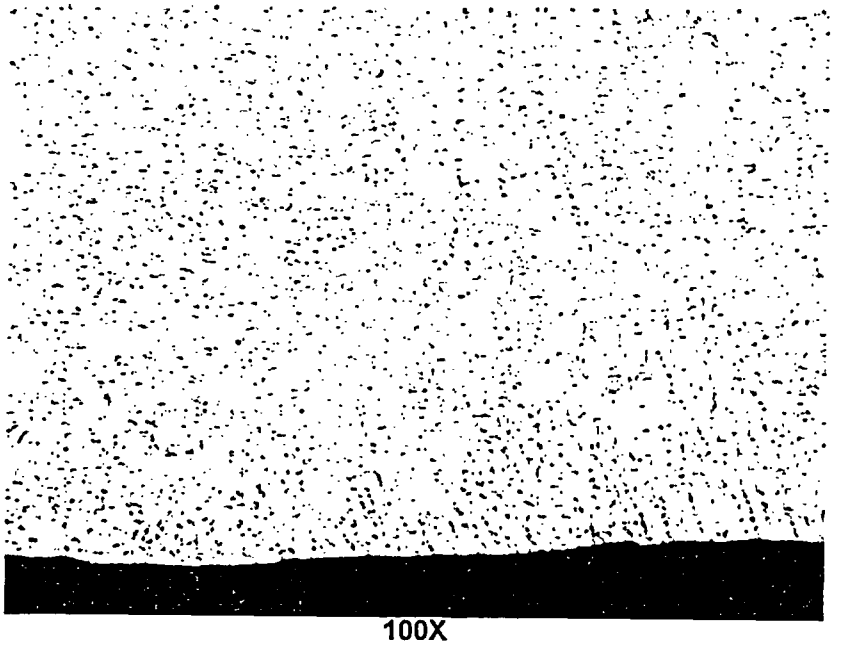

100X

375X

Figure 6.1.1.5: Typical clad microstructure near RCS side surface of the cladding. No intergranular attack (IGA) was present.

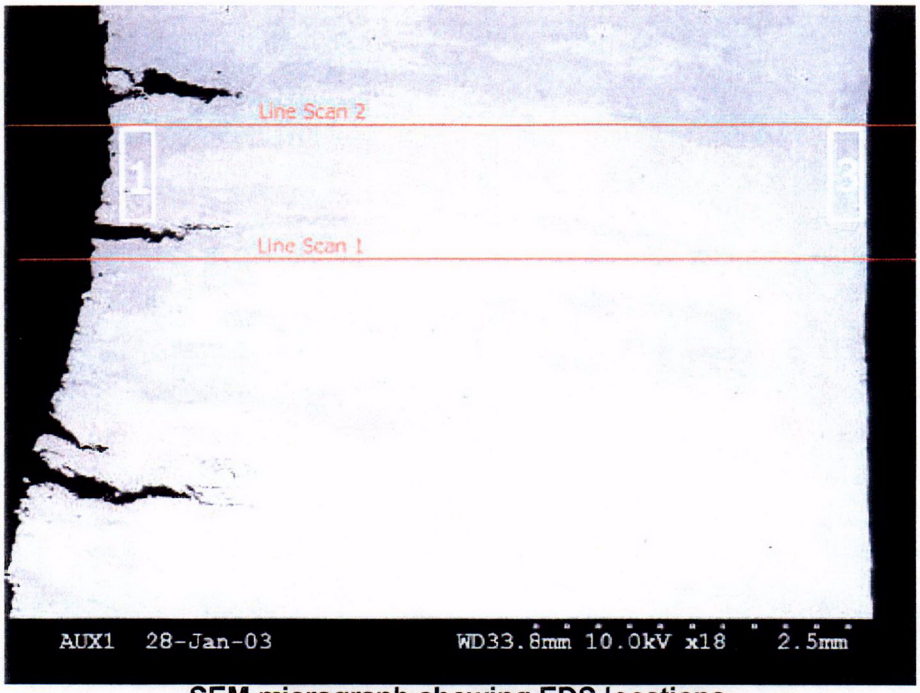

SEM micrograph showing EDS locations.

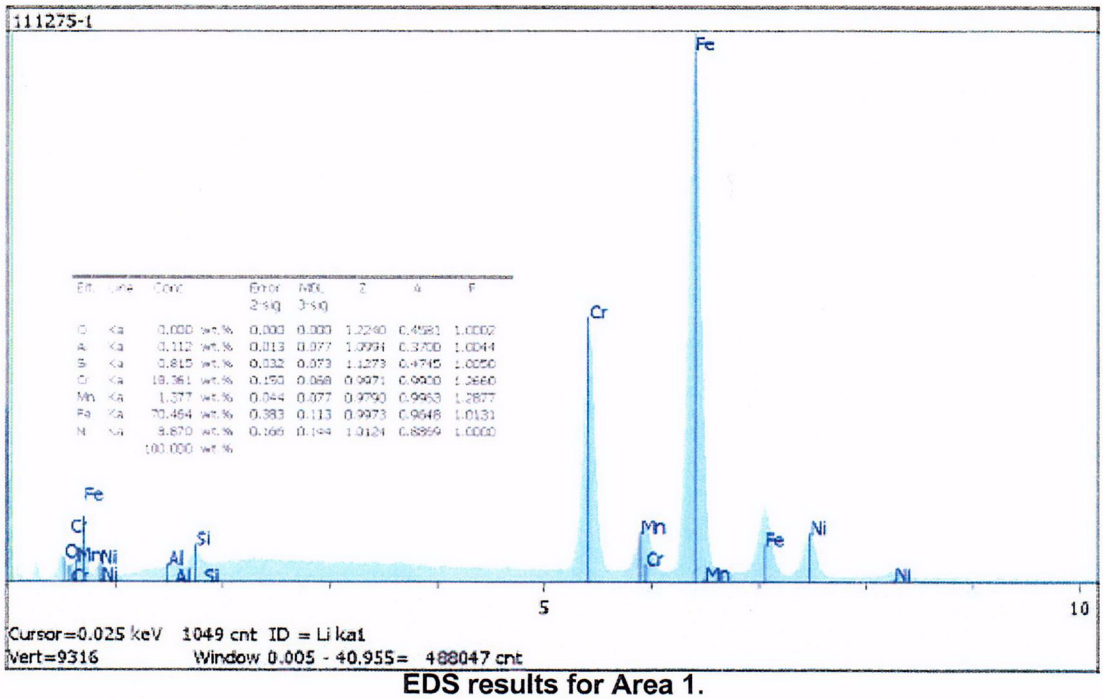

EDS results for Area 1.

Figure 6.1.2.1: SEM micrograph showing the three deepest cracks in A2A7M. Crack tips are 0.042" to 0.069" (1.1 to 1.75 mm) below the surface. It is noted that these three crack tips are at approximately the same distance of 0.199" (5.06 mm) from the underside surface. EDS scans of areas 1, 2, and 3 and line scans 1 and 2 (not included) indicated a generally uniform chemical composition (including Cr content) across the cladding thickness.

C51

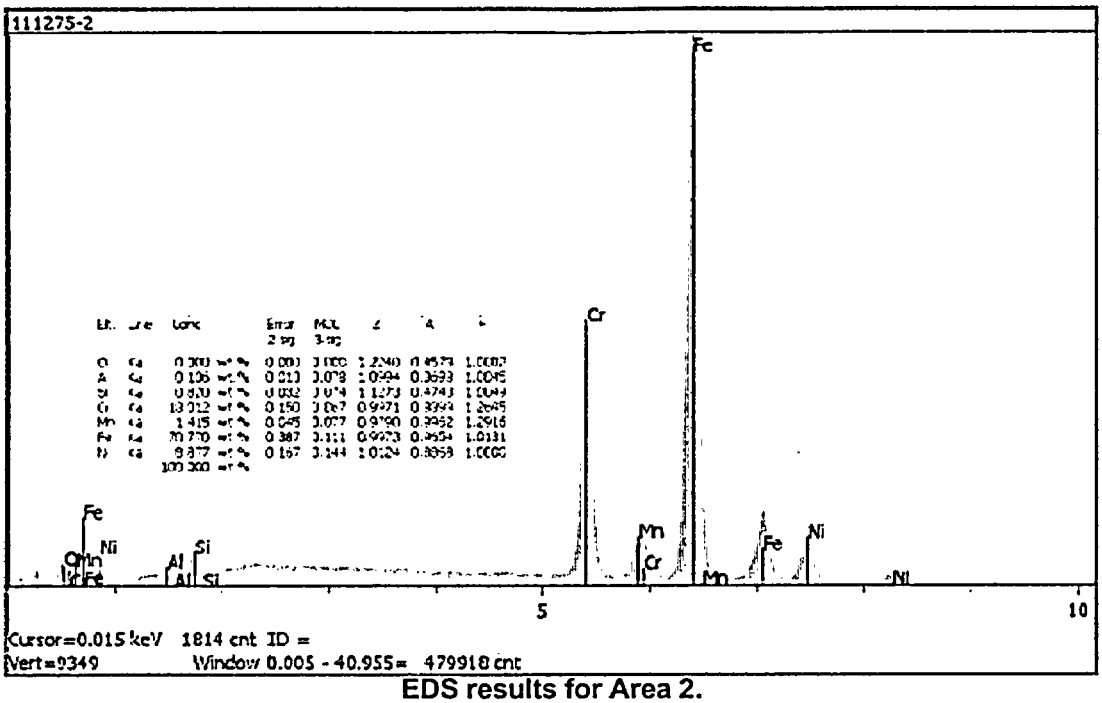

EDS results for Area 2.

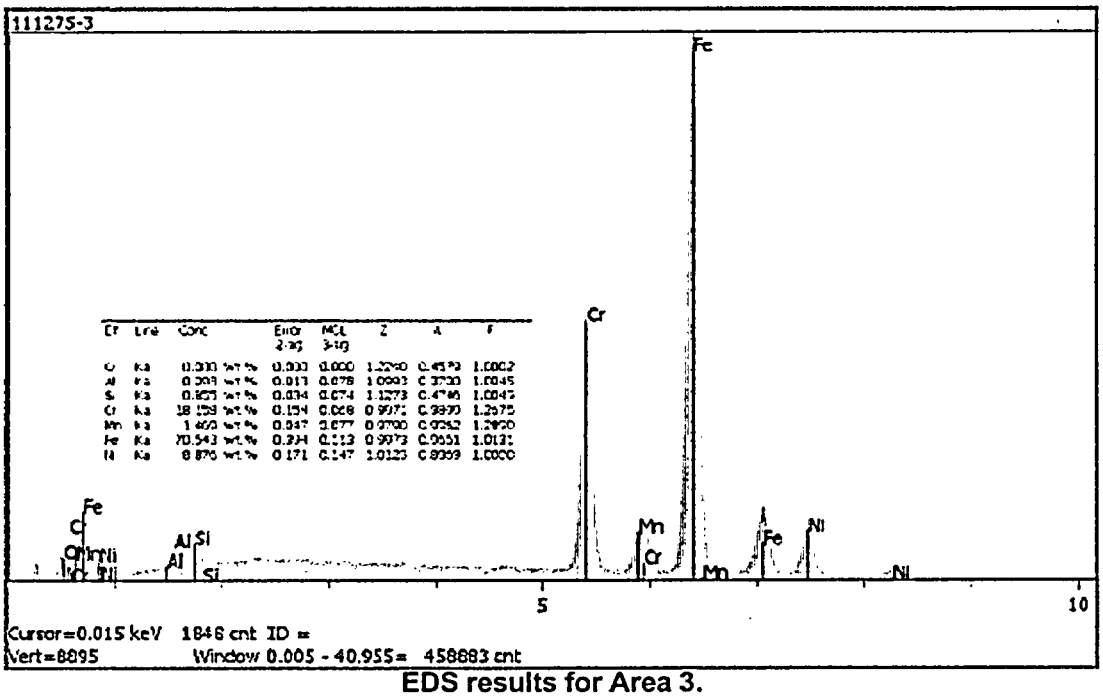

EDS results for Area 3.

Figure 6.1.2.1 (cont.): EDS results for Areas 2 and 3.

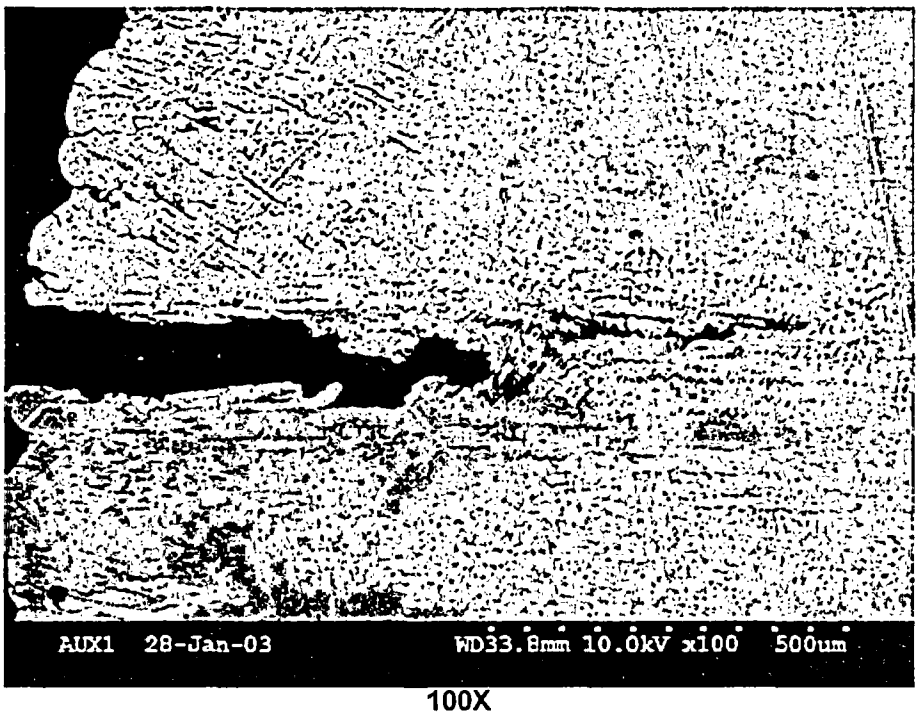

100X

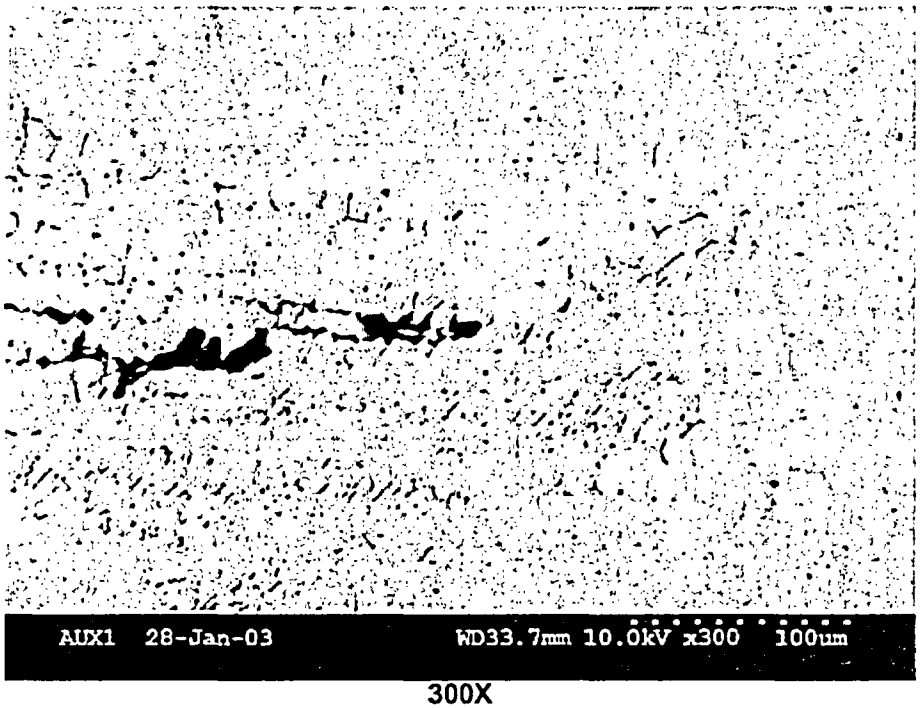

300X

Figure 6.1.2.2: SEM micrographs showing interdendritic crack path along the elongated ferrite pools.

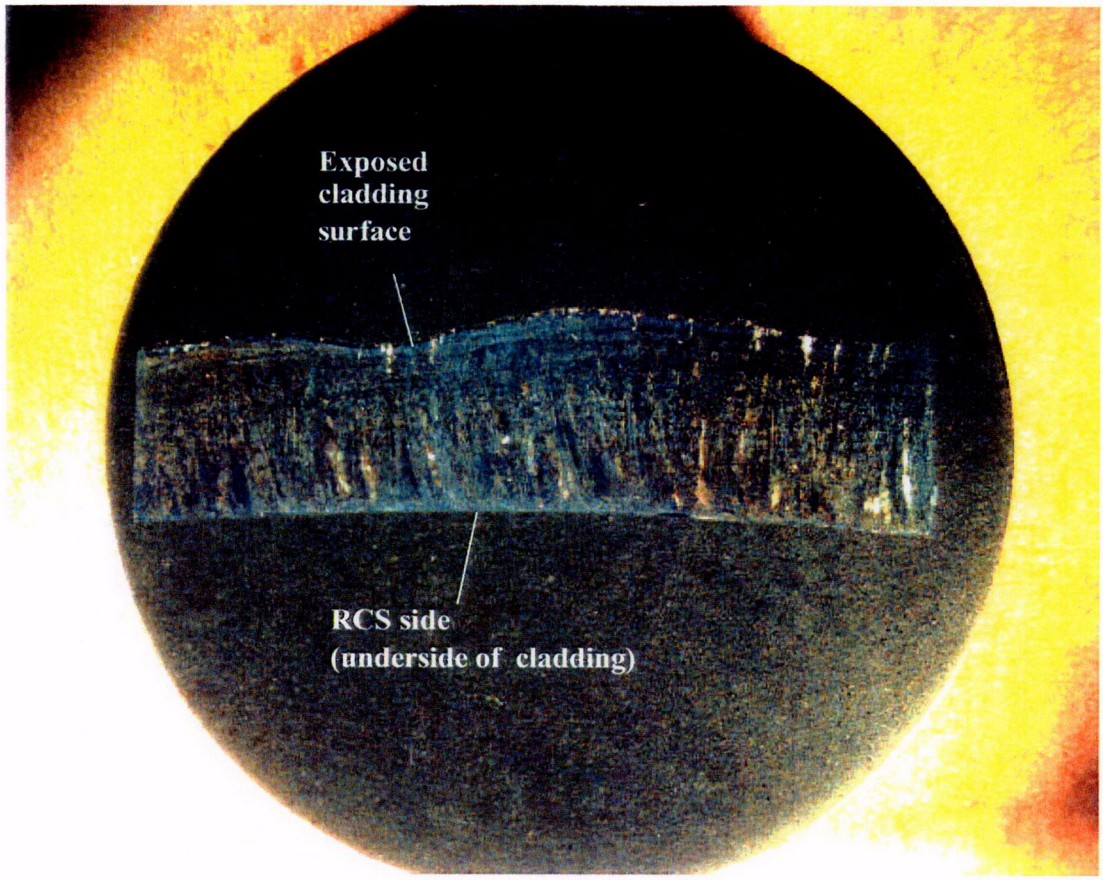

Figure 6.2.1.1: 4X macro photograph of metallurgical mount A2A7N.
Refer to Figure 5.11 for the sample orientation.

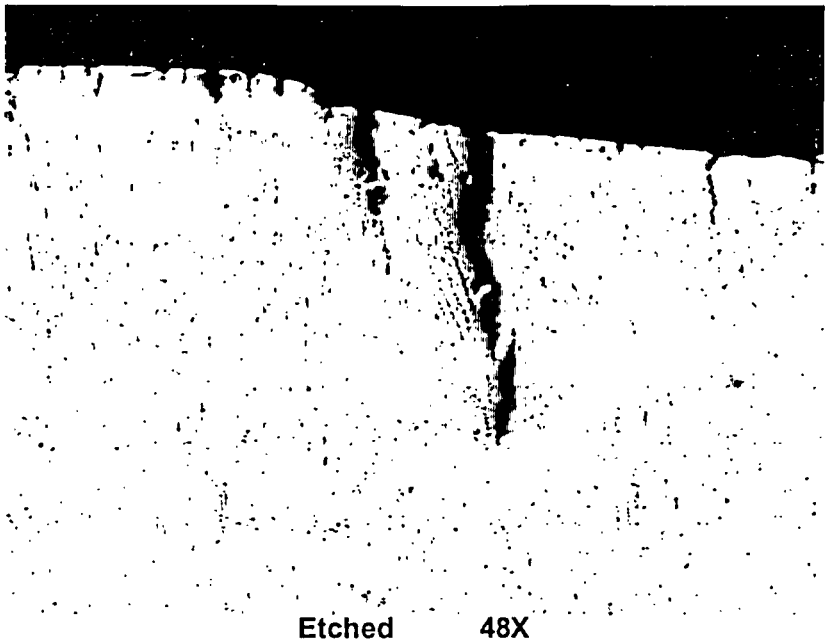

Figure 6.2.1.2: Micrograph of a crack observed on A2A7N. The crack tip is estimated to be approximately 0.036" (0.91 mm) below the surface.

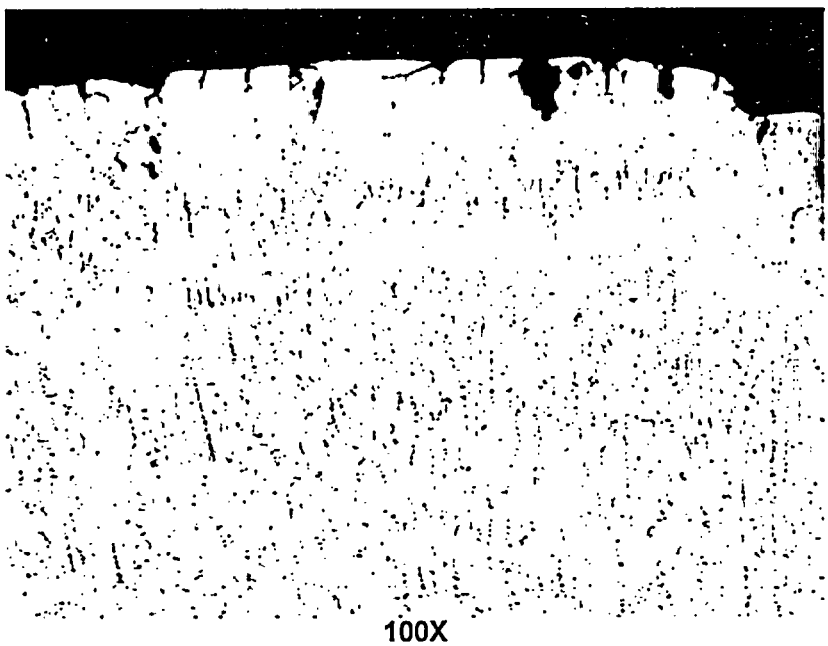

100X

375X

Figure 6.2.1.3: Micrographs showing intergranular attack (IGA) and intergranular cracking on the exposed stainless steel cladding.

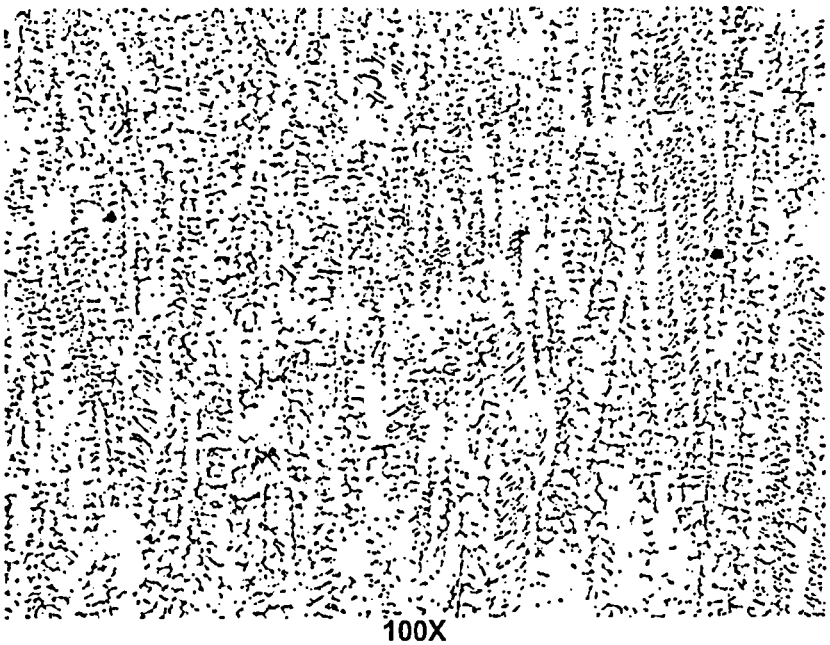

100X

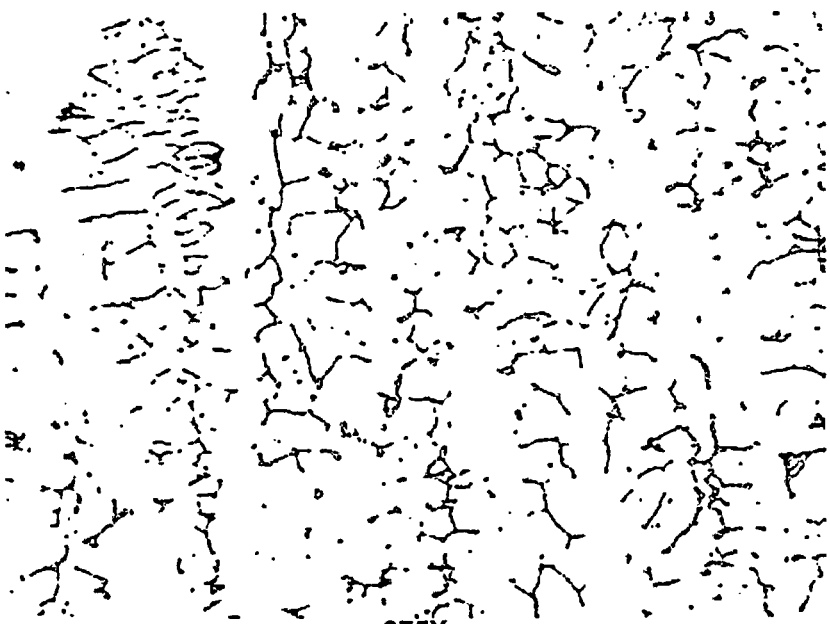

375X

Figure 6.2.1.4: Typical clad microstructure in the mid-thickness of the cladding.

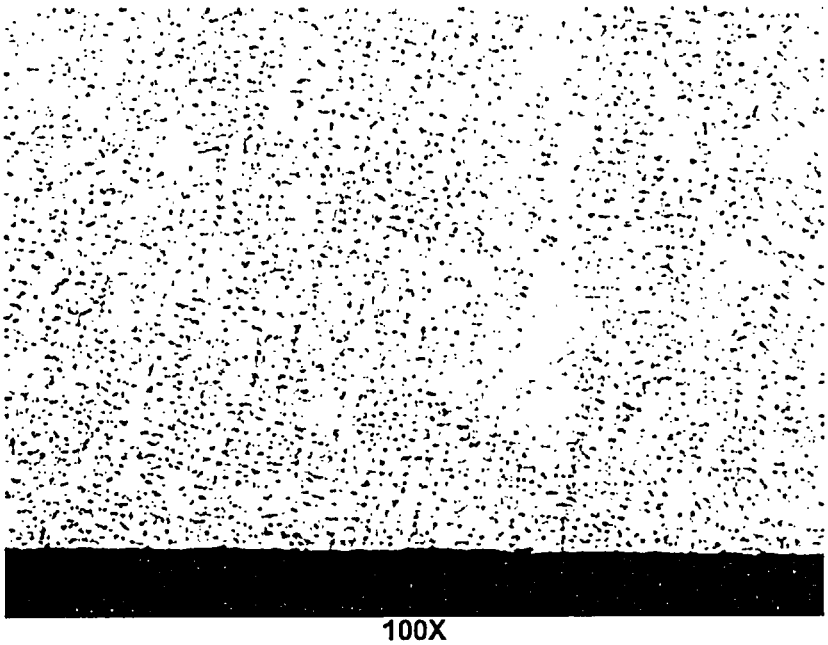

100X

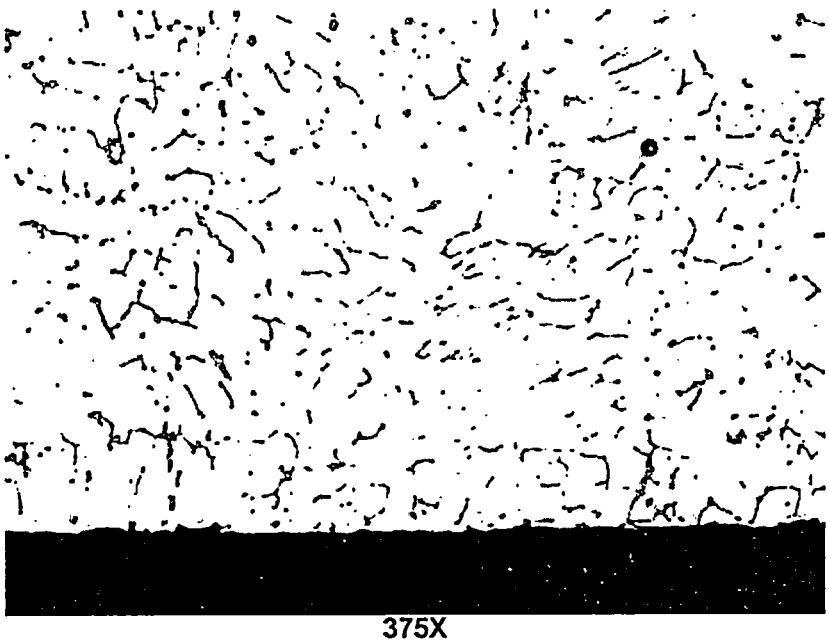

375X

Figure 6.2.1.5: Typical clad microstructure near RCS side surface of the cladding. No intergranular attack (IGA) was present.

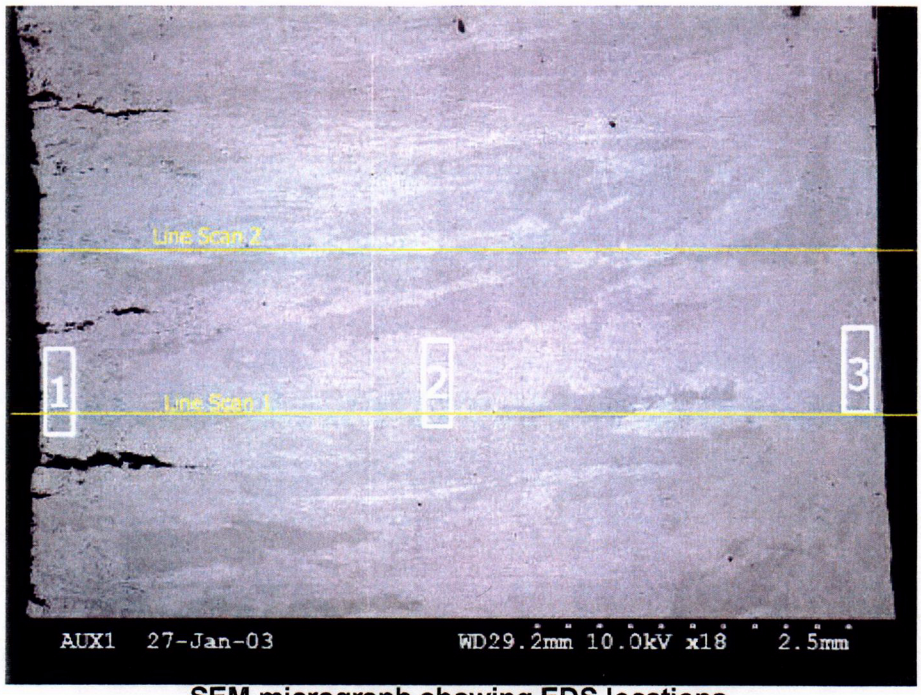

SEM micrograph showing EDS locations.

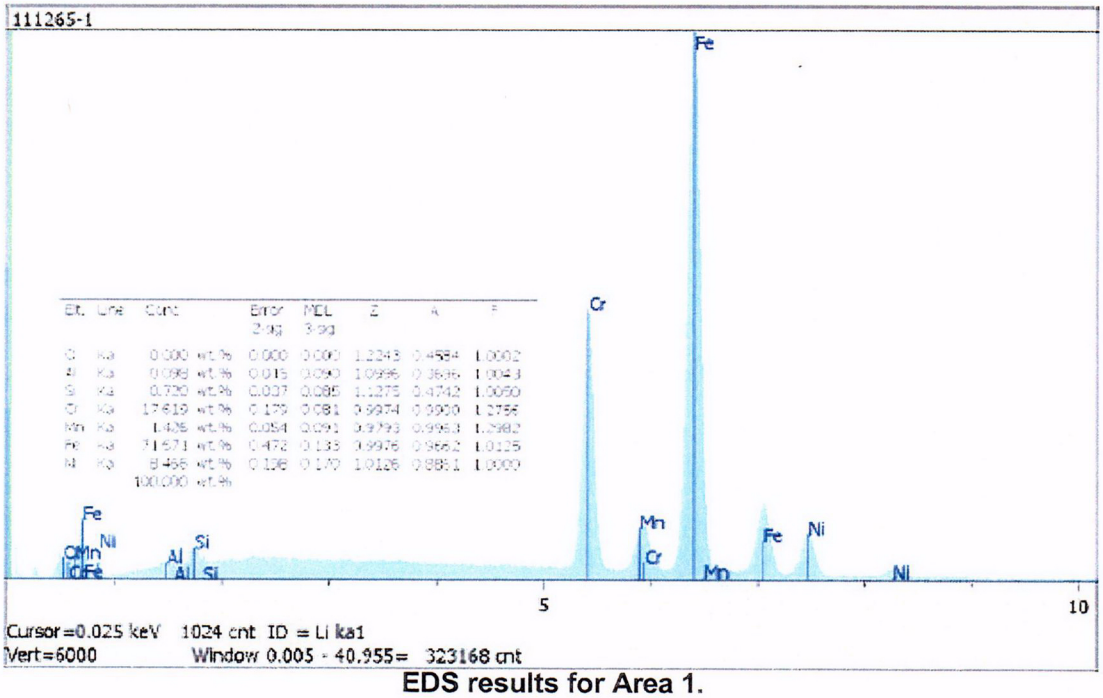

EDS results for Area 1.

Figure 6.2.2.1: SEM micrograph showing the three deepest cracks in A2A7N. The maximum crack depth was approximately 0.056" (1.42 mm). EDS scans of areas 1, 2, and 3 and lines 1 and 2 (not included) indicated a generally uniform chemical composition (including Cr content) across the cladding thickness.

C53

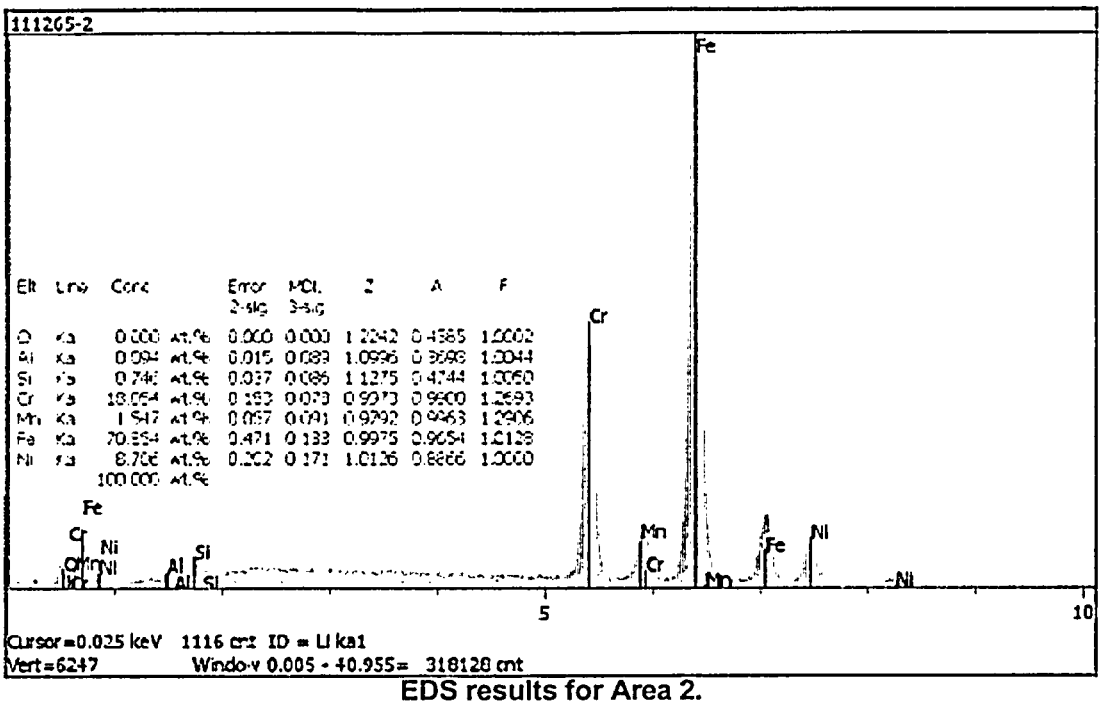

EDS results for Area 2.

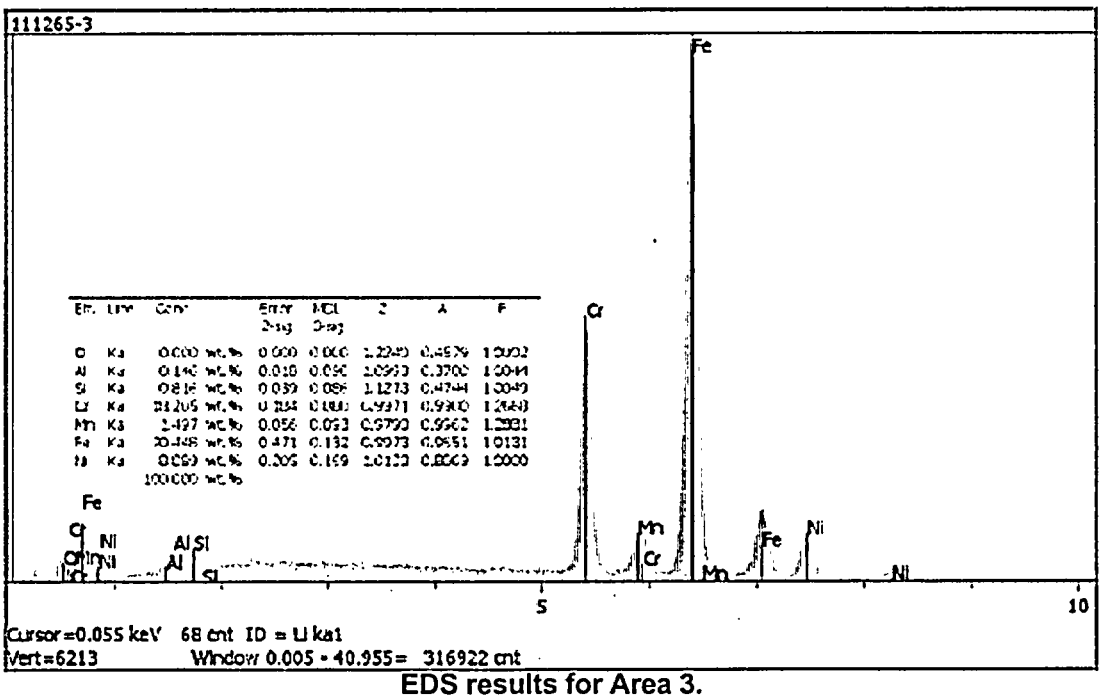

EDS results for Area 3.

Figure 6.2.2.1 (cont.): EDS results for Areas 2 and 3.

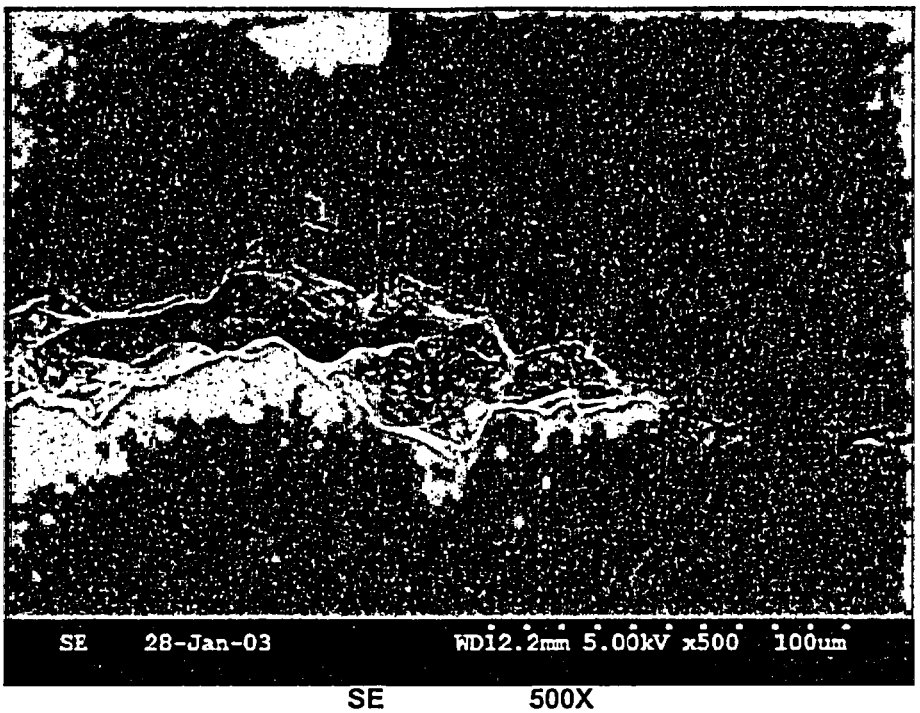

SE 500X

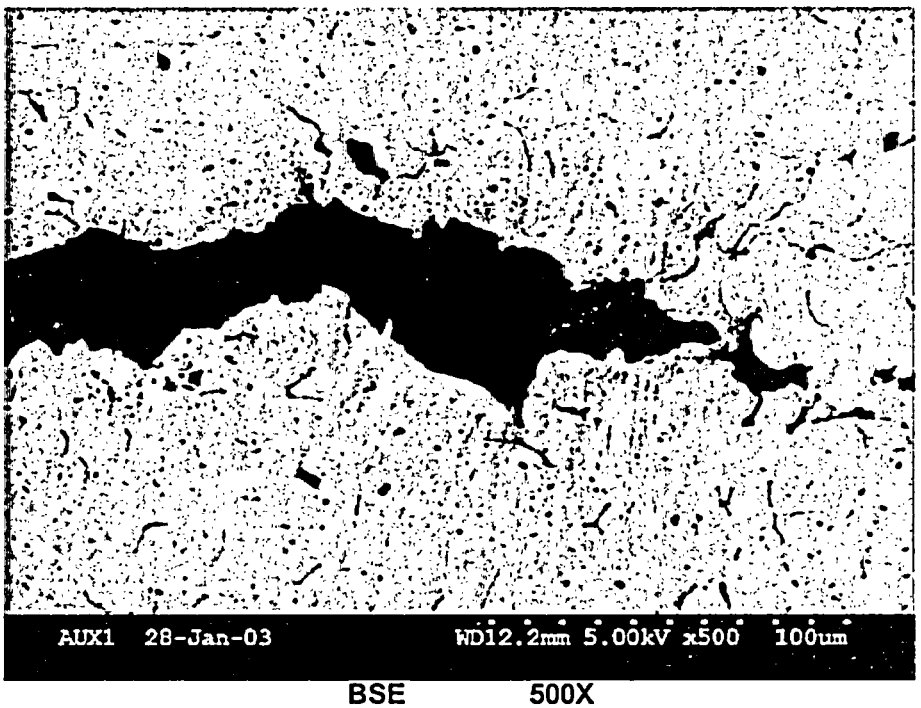

BSE 500X

Figure 6.2.2.2: Higher magnification SEM micrographs of crack tip, showing the interdendritic crack path along the elongated ferrite pools.

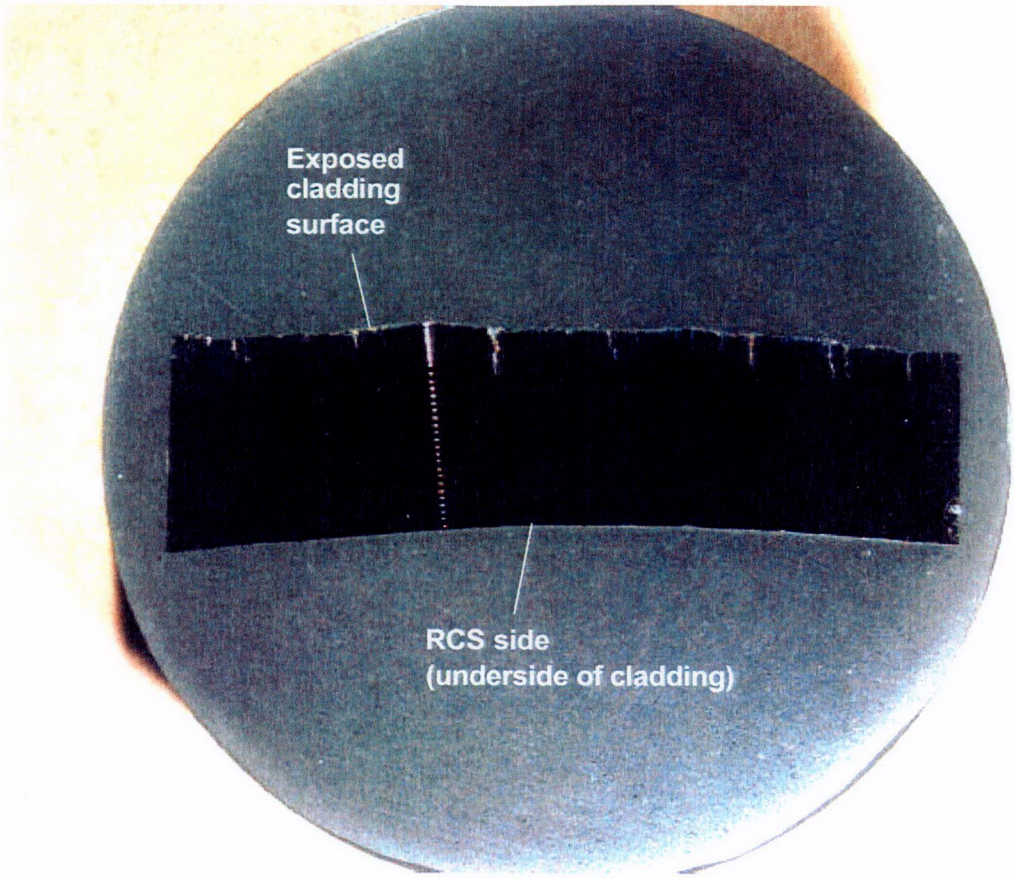

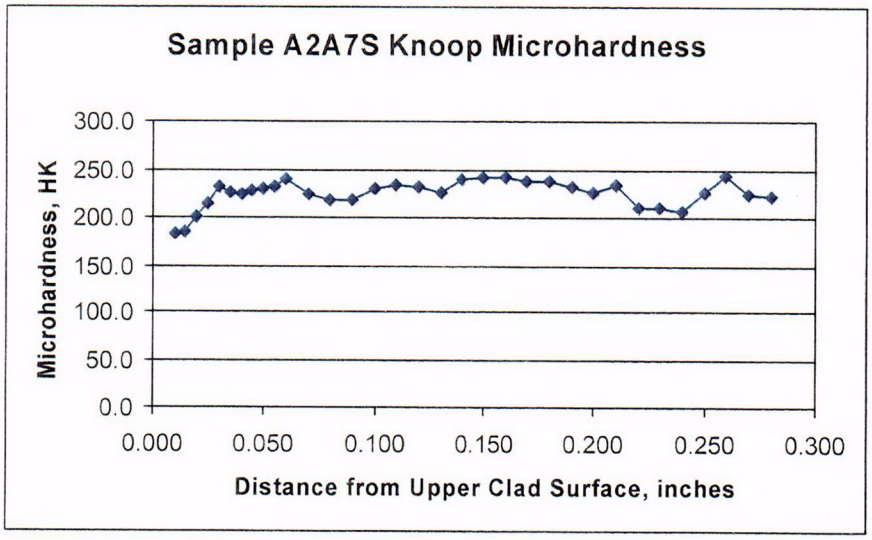

Figure 6.3.1.1: 4X macro photograph of metallurgical mount A2A7S. Refer to Figure 5.11 for the sample orientation. Knoop microhardness values exhibited lower hardness readings toward the exposed clad side (left side of graph), which was in contrast to A2A7M.

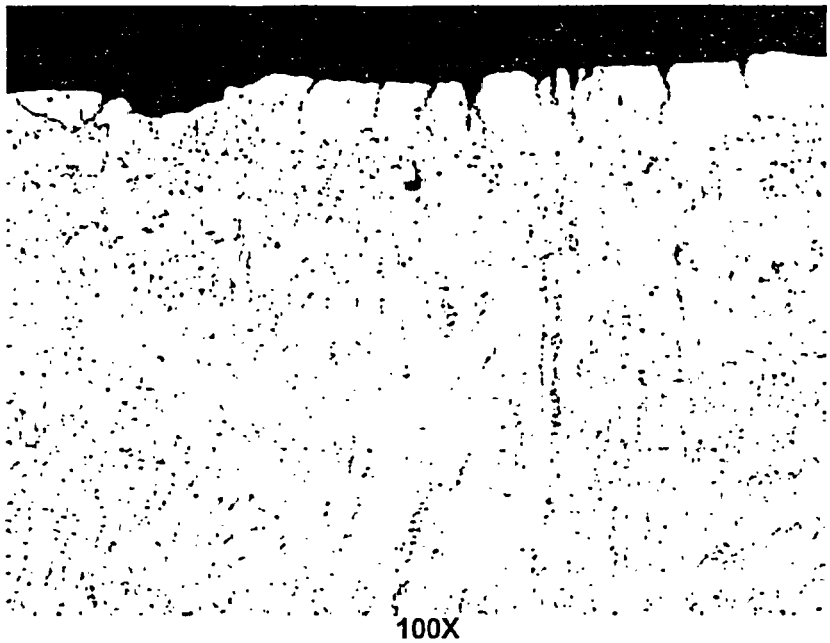

100X

375X

Figure 6.3.1.2: Micrographs showing intergranular attack (IGA) and intergranular or interdendritic cracking on the exposed stainless steel cladding.

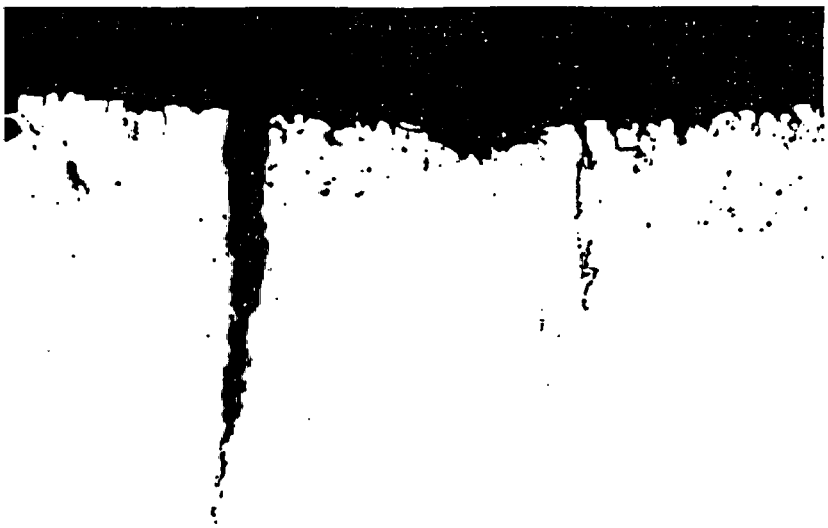

As-polished 48X

Etched 48X

Figure 6.3.1.3: Micrographs of cracking observed on sample A2A7S. Different cracks are shown.

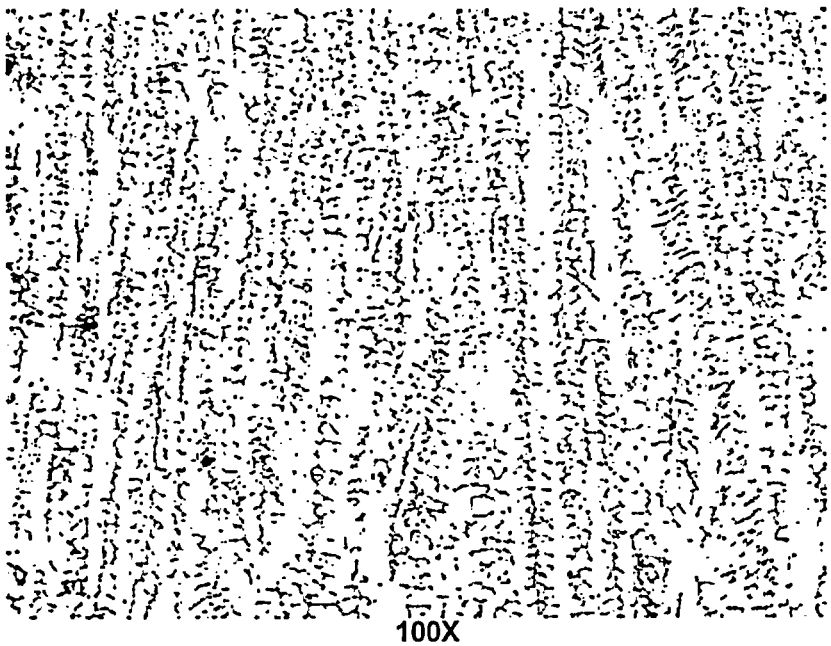

100X

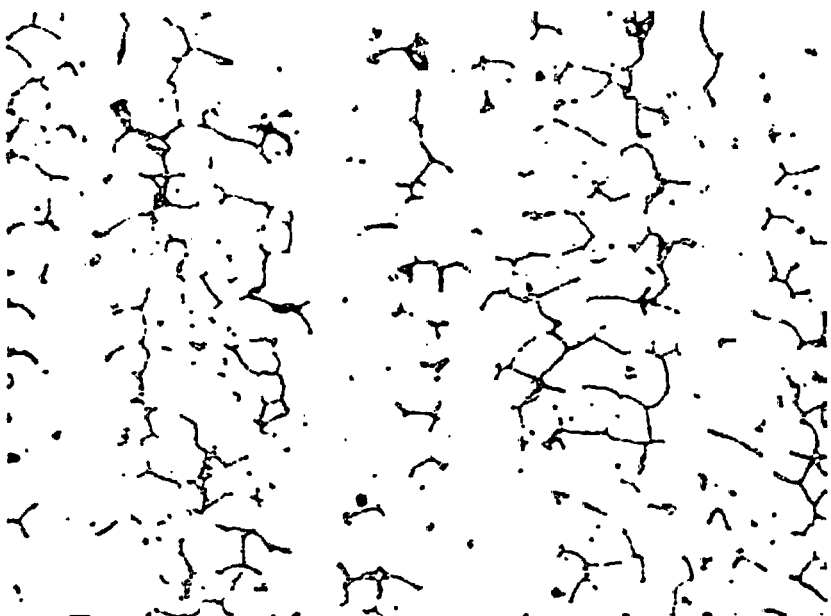

375X

Figure 6.3.1.4: Typical clad microstructure in the mid-thickness of the cladding.

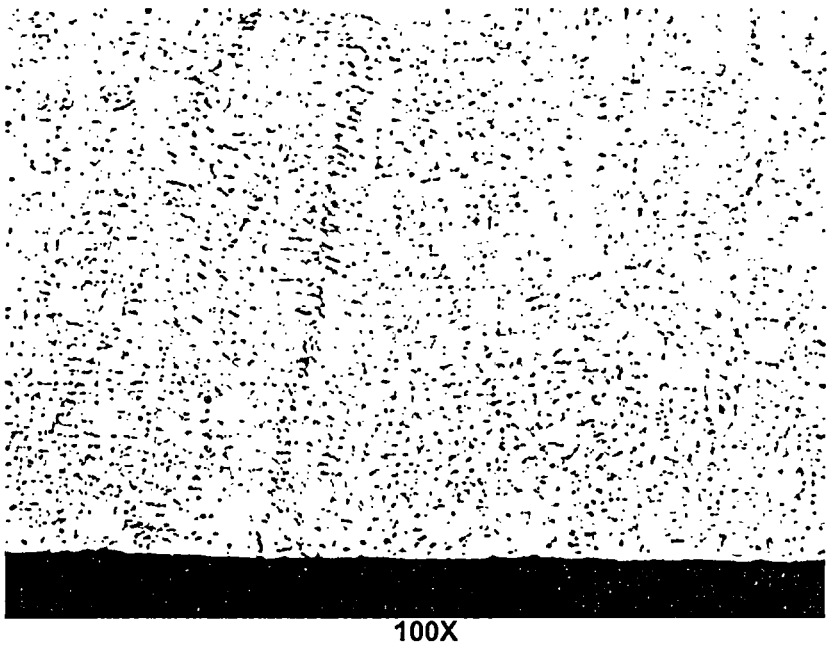

100X

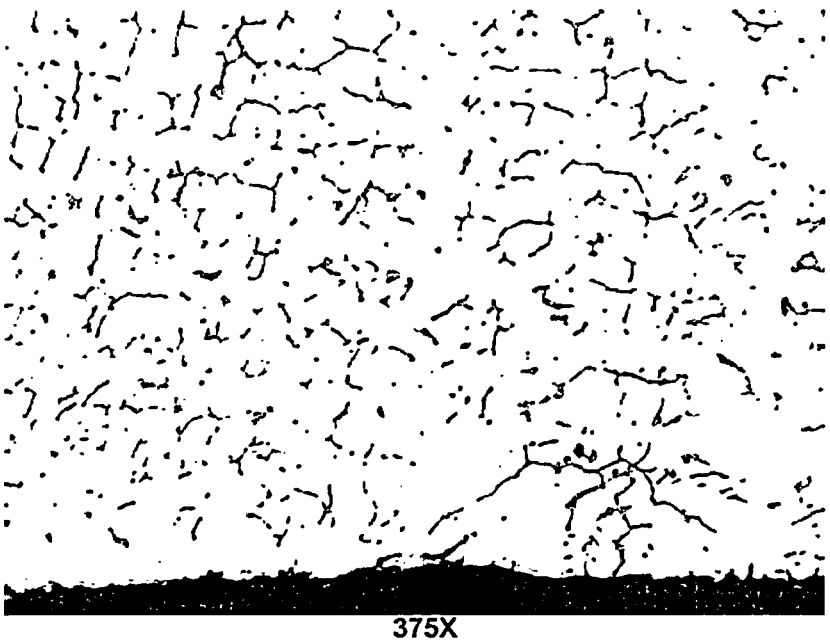

375X

Figure 6.3.1.5: Typical clad microstructure near RCS side surface of the cladding. No intergranular attack (IGA) was present.

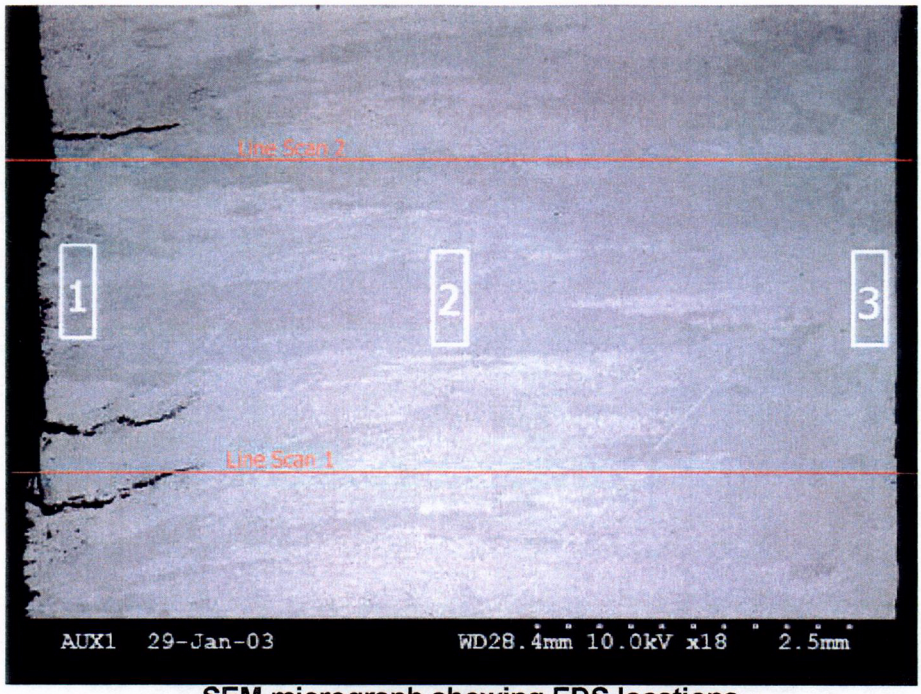

SEM micrograph showing EDS locations.

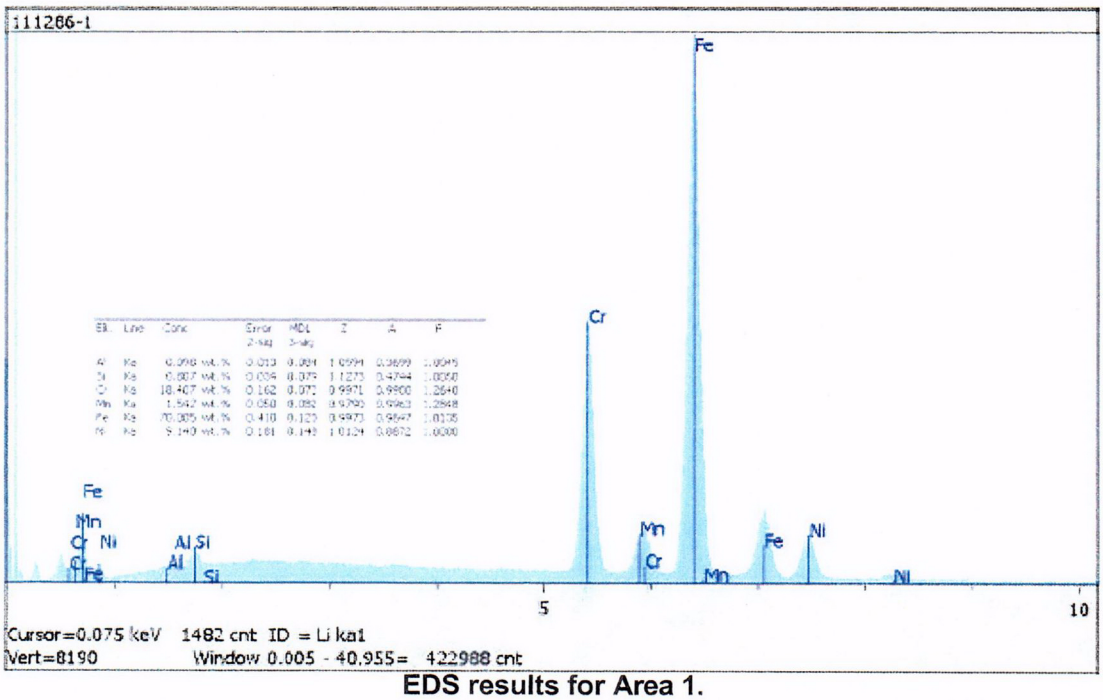

EDS results for Area 1.

Figure 6.3.2.1: SEM micrograph of the three deepest cracks in A2A7S. The maximum crack depth was approximately 0.056" (1.42 mm). These three crack tips are approximately the same distance from the underside surface. EDS scans of areas 1, 2, and 3 and lines 1 and 2 (not included) indicated a generally uniform chemical composition (including Cr content) across the cladding thickness.

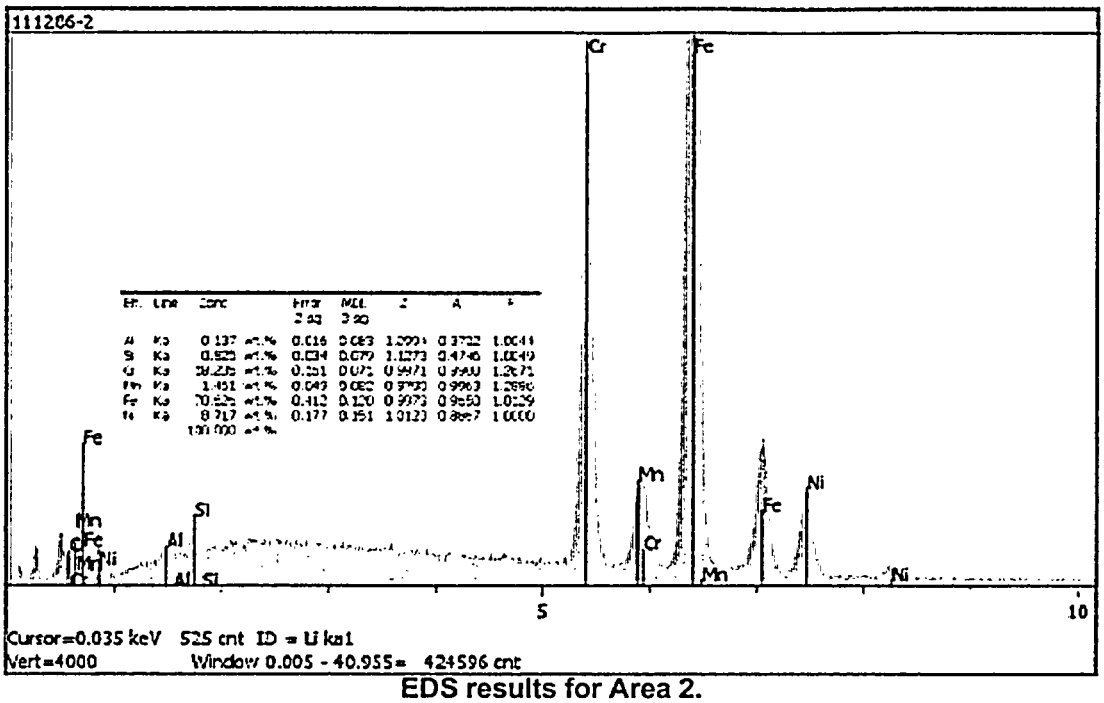

EDS results for Area 2.

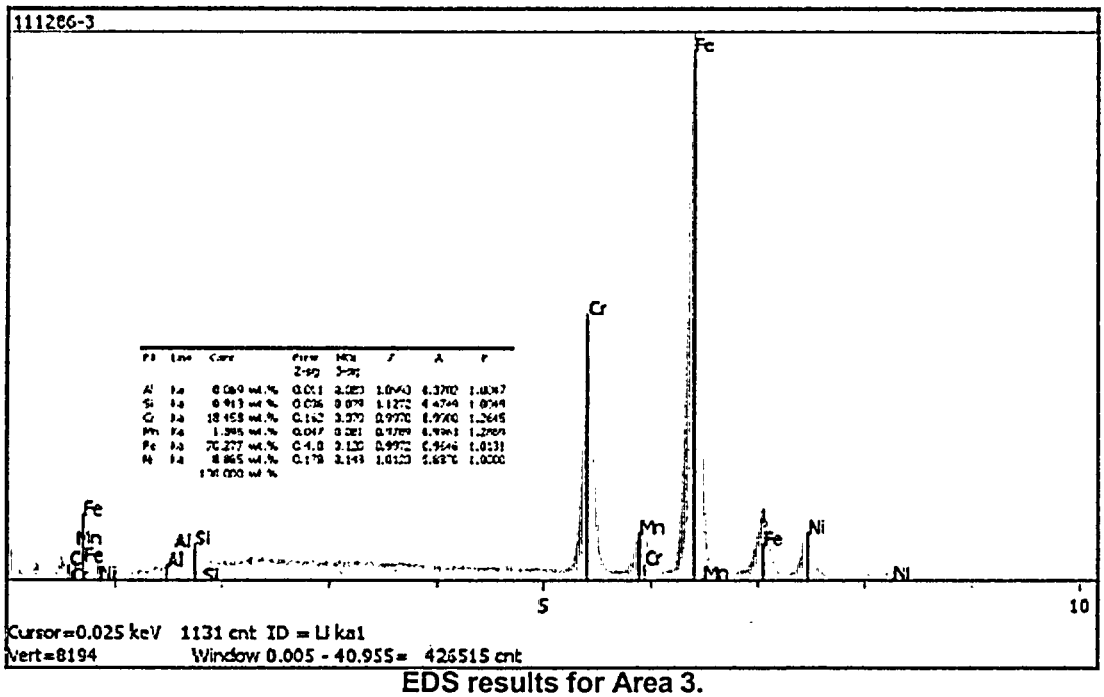

EDS results for Area 3.

Figure 6.3.2.1 (cont.): EDS results for Areas 2 and 3. Note that the Cr peak was set at full screen height for Area 2.

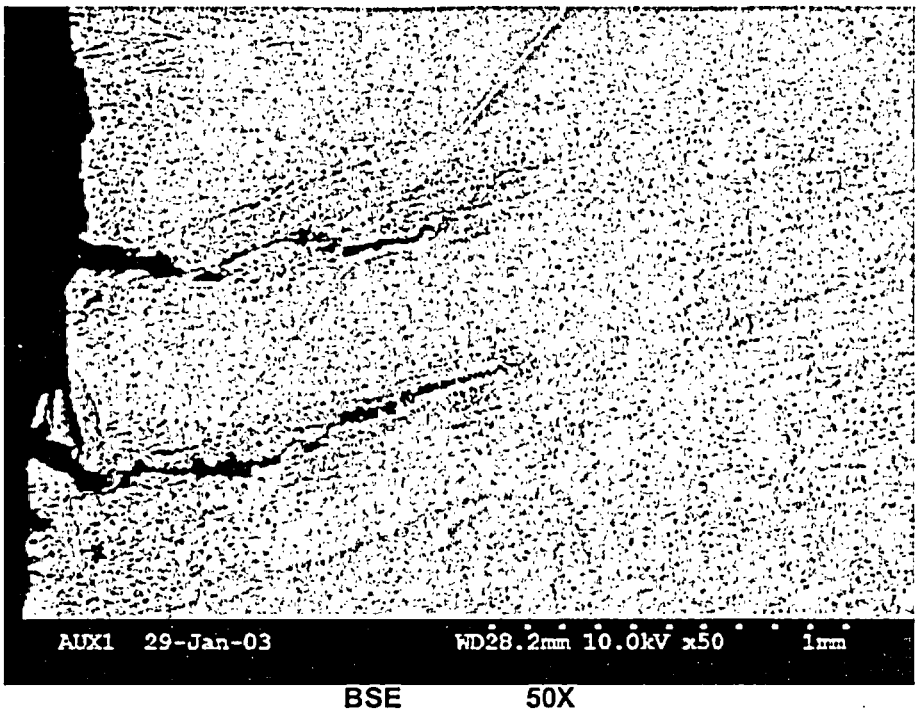

BSE 50X

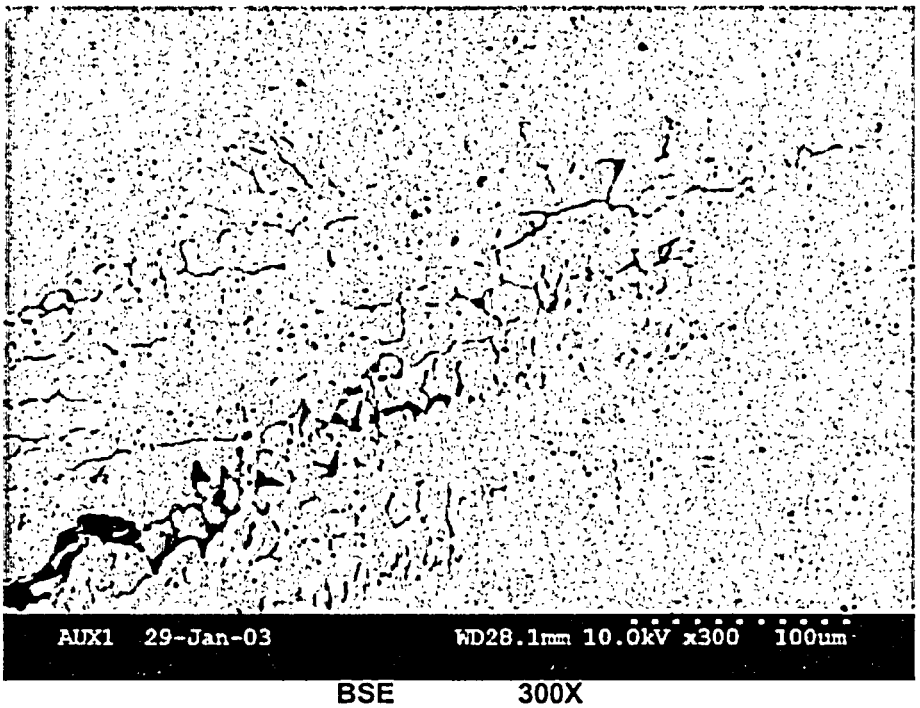

BSE 300X

Figure 6.3.2.2: Higher magnification SEM micrographs of crack tip, showing the interdendritic crack path along the elongated ferrite pools.

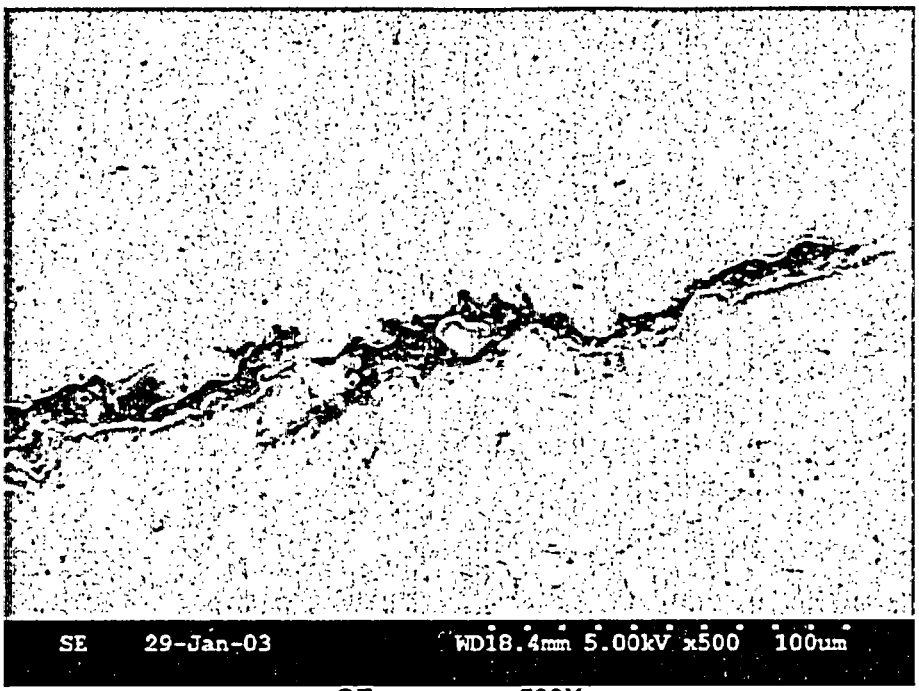

SE 500X

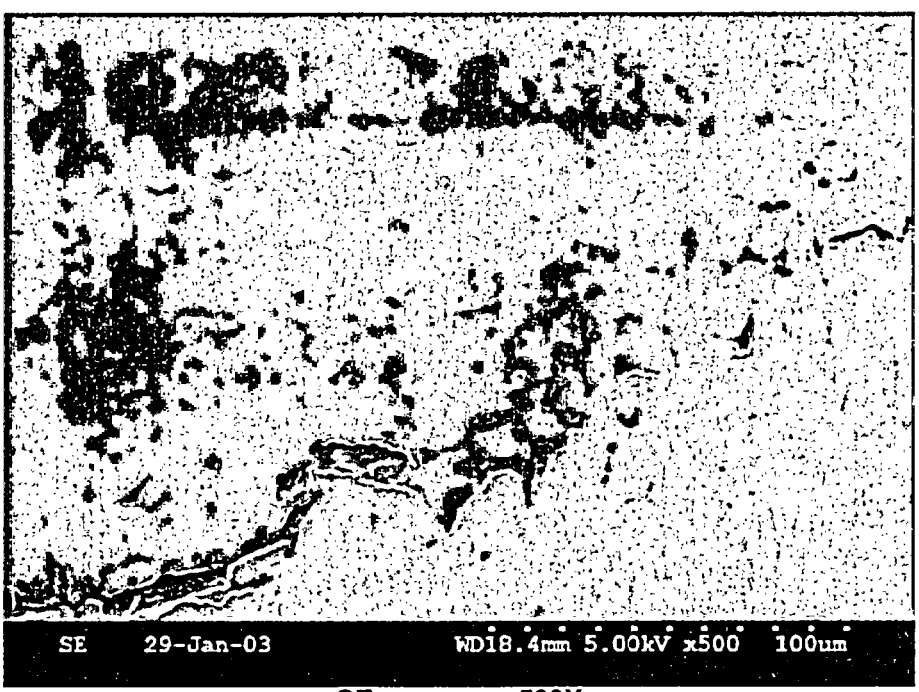

SE 500X

Figure 6.3.2.3: Secondary electron SEM images of crack tip, showing the interdendritic crack path along the elongated ferrite pools.

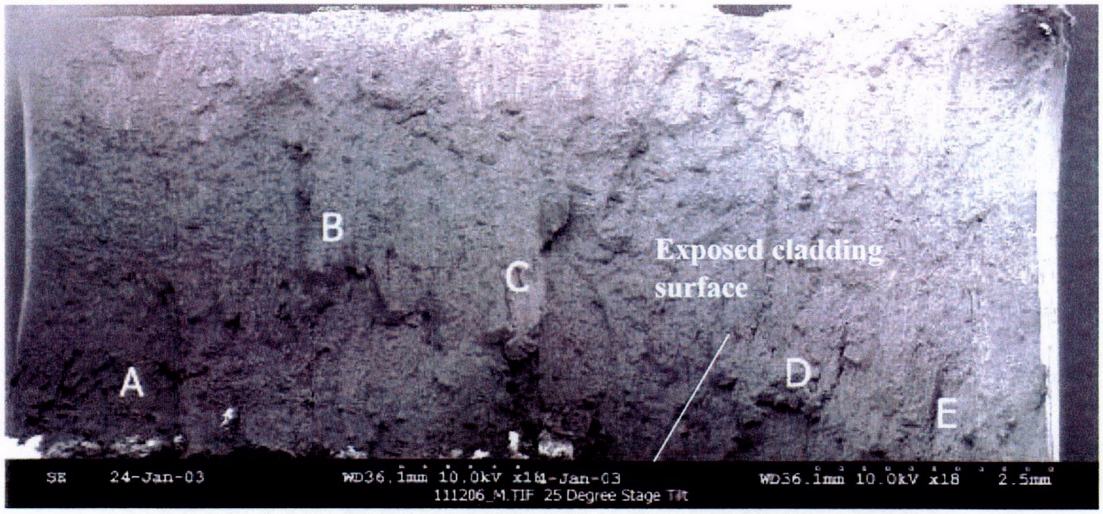

Figure 6.4.1.1: Low magnification SEM mosaic showing the opened main crack (sample A2A7-L1A). Refer to Figures 5.11 and 5.12 for the sample location. The exposed cladding surface is oriented downward in the SEM micrographs.

C56

BSE 50X

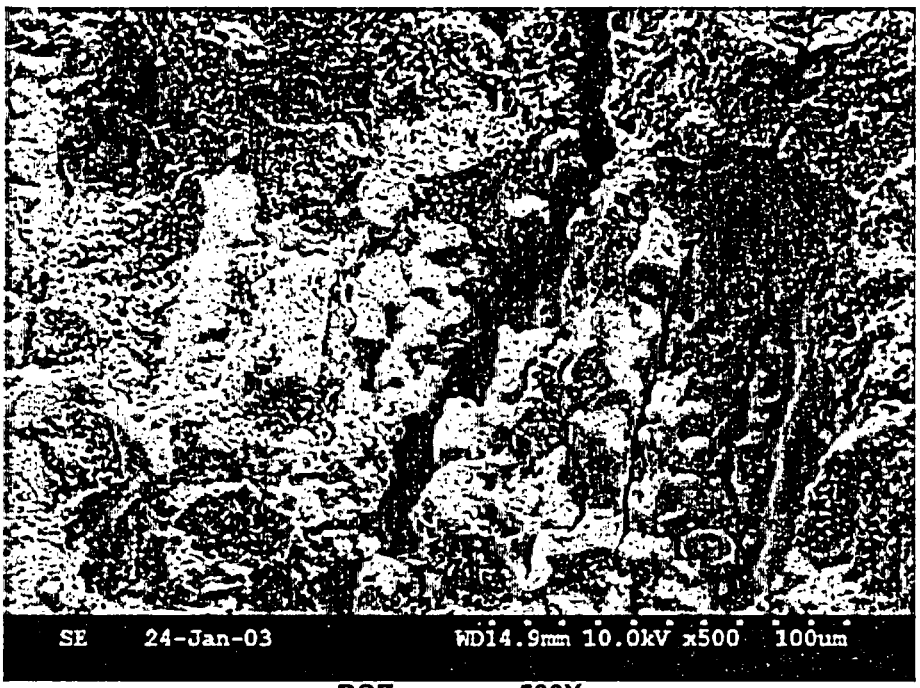

BSE 500X

Figure 6.4.1.2: Near mosaic area "A". Heavy deposits are present toward the exposed side of the cladding (darker contrast in BSE micrograph). Fracture morphology is interdendritic in nature.

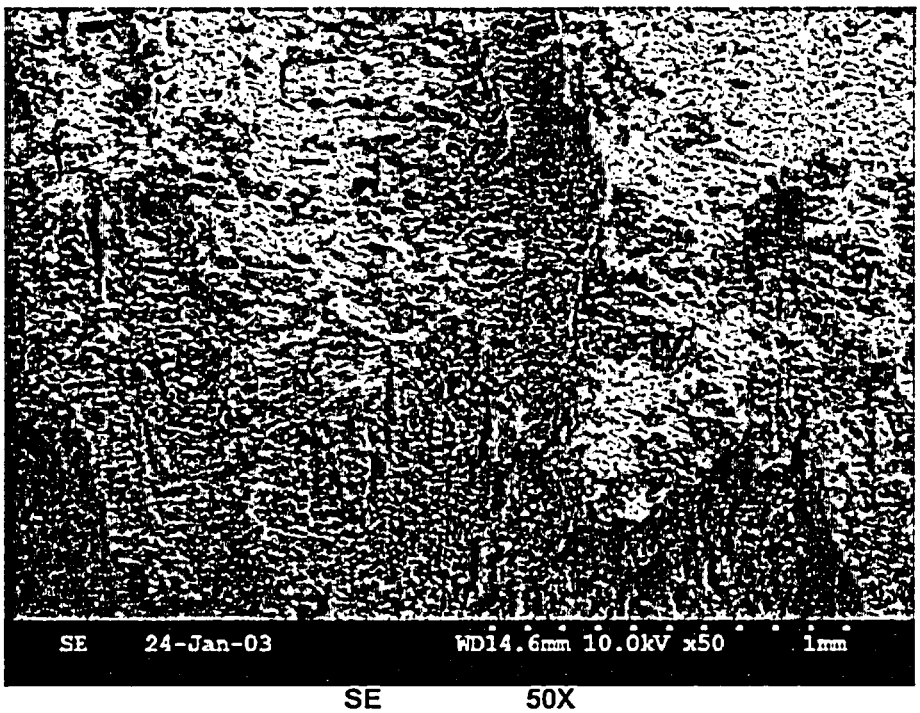

SE 50X

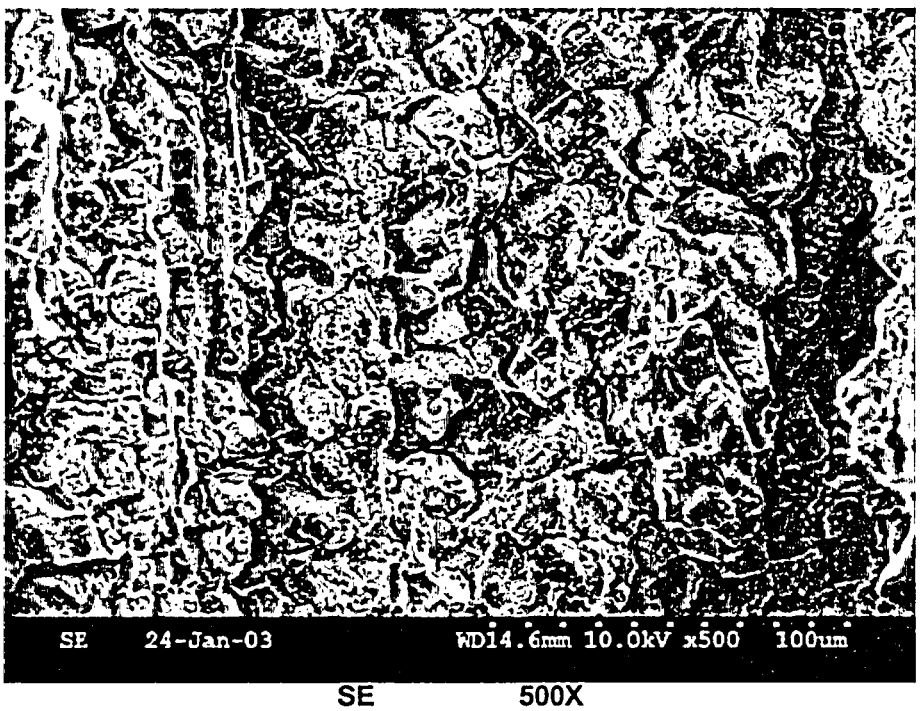

SE 500X

Figure 6.4.1.3: Near mosaic area "B". Cracking is intergranular/interdendritic.

BSE 150X

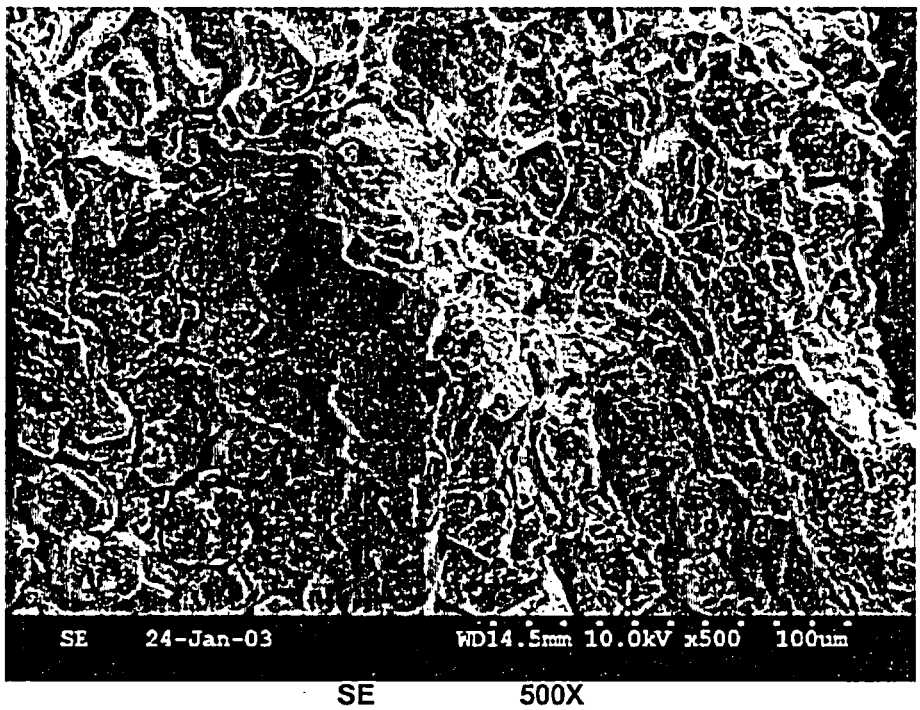

SE 500X

Figure 6.4.1.4: Near mosaic area "C". Fracture mode is intergranular or interdendritic for in-service cracking and ductile tearing for lab opened-up fracture.

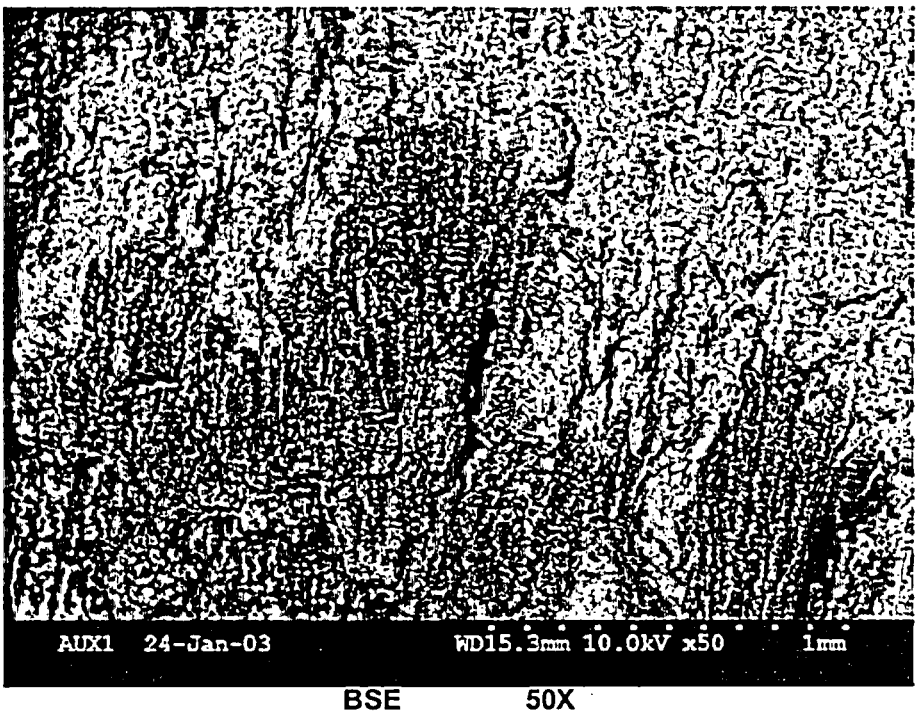

BSE 50X

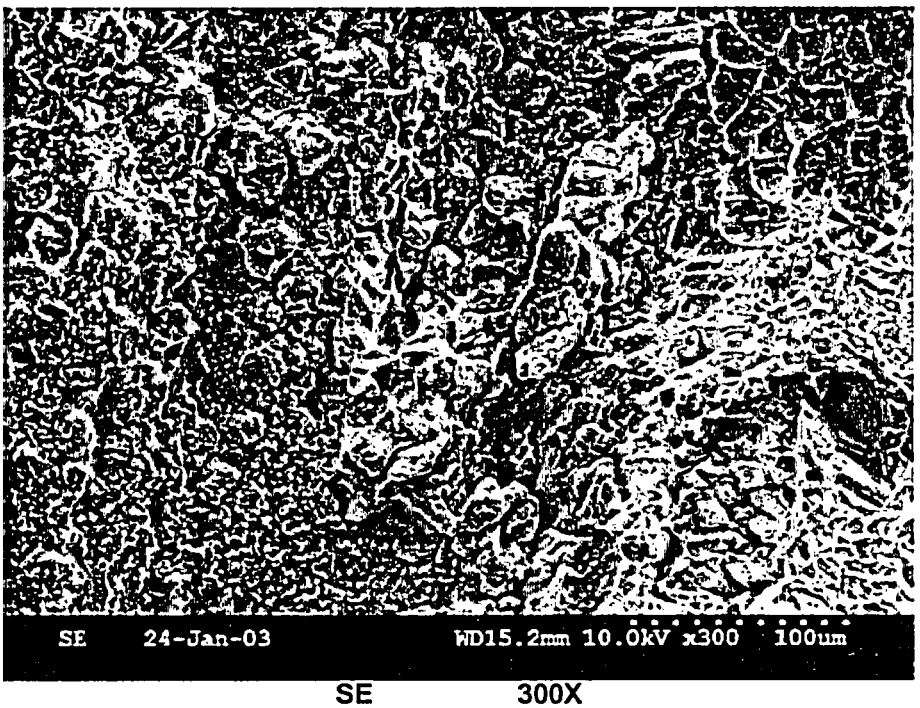

SE 300X

Figure 6.4.1.5: Near mosaic area "D". Fracture mode is intergranular or interdendritic for in-service cracking and ductile tearing for lab opened-up fracture (upper right).

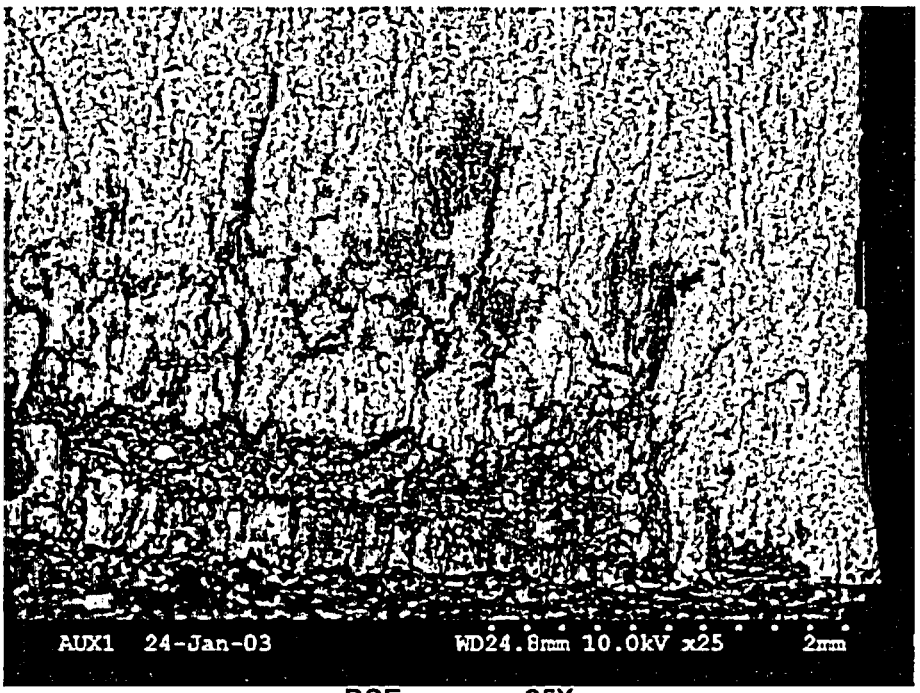

BSE 25X

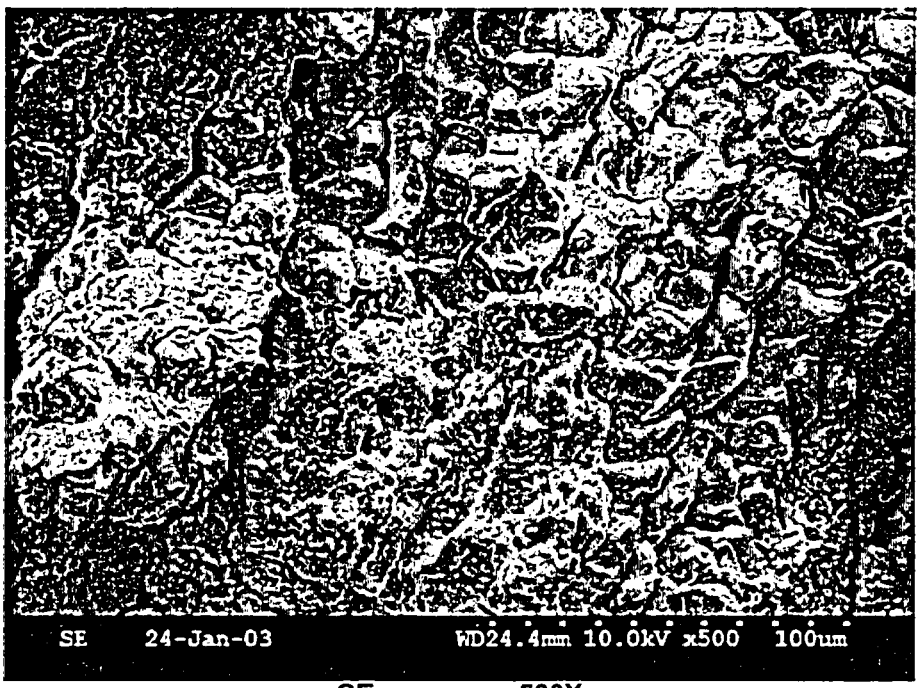

SE 500X

Figure 6.4.1.6: Near mosaic area "E". Cracking is intergranular/interdendritic.

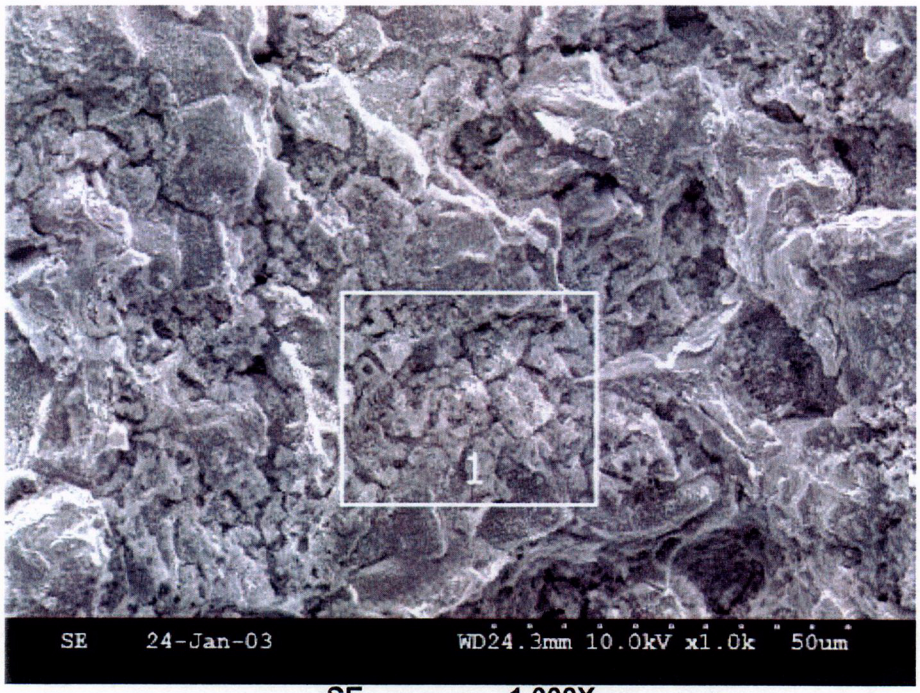

SE 1,000X

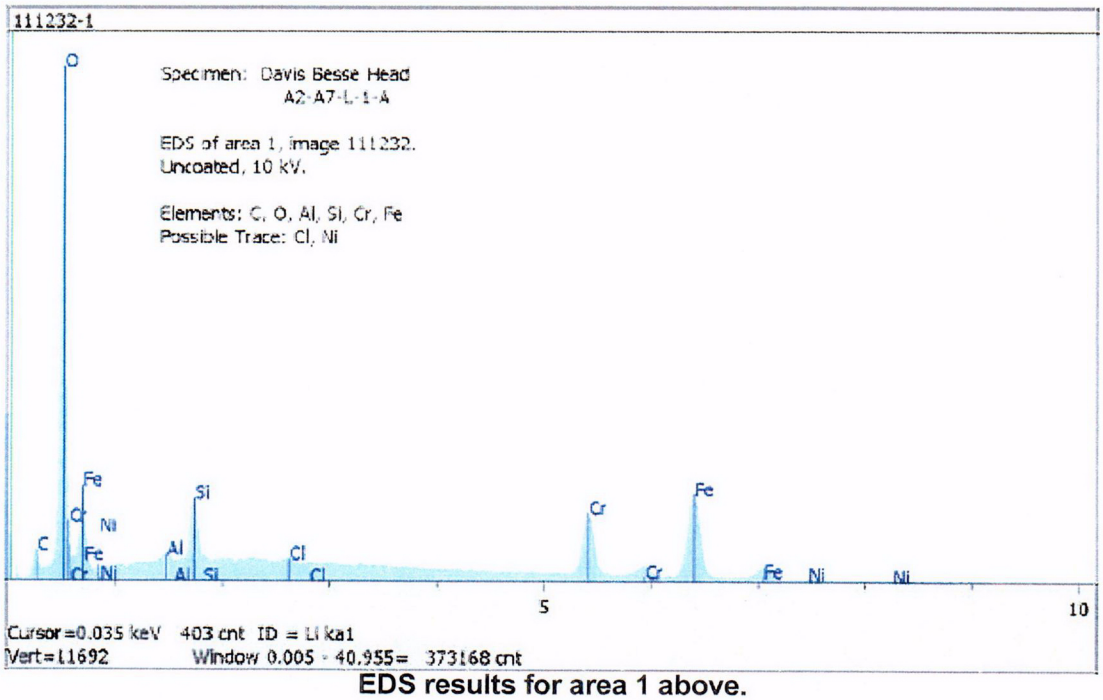

EDS results for area 1 above.

Figure 6.4.1.7: SEM micrograph and EDS results for deposited region near area "E". The corrosion deposits contained carbon, oxygen, along with iron, aluminum, silicon, and chromium. Possible trace levels of nickel and chlorine were also detected in this area.

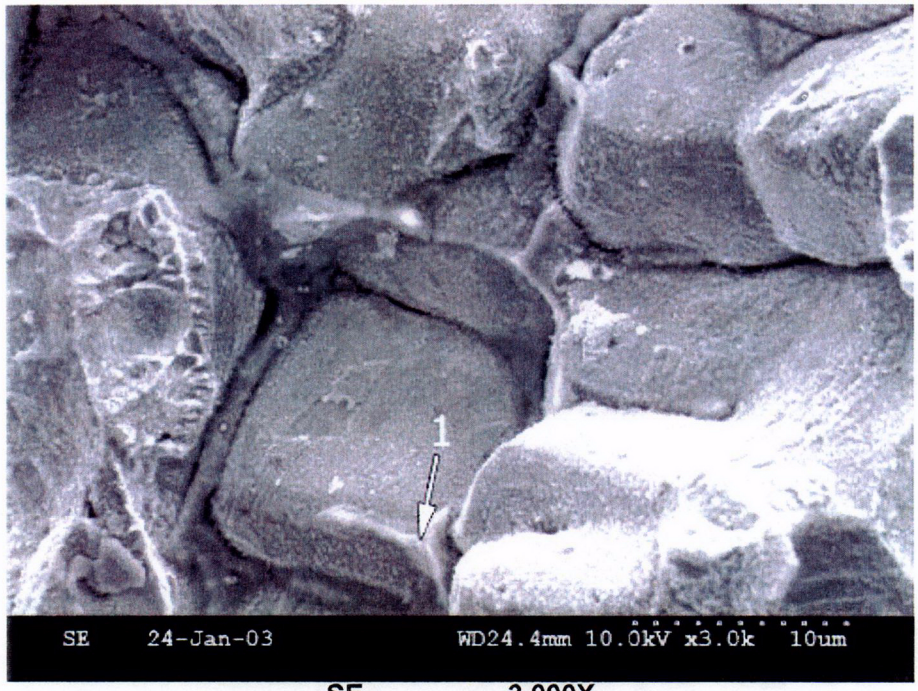

SE 3,000X

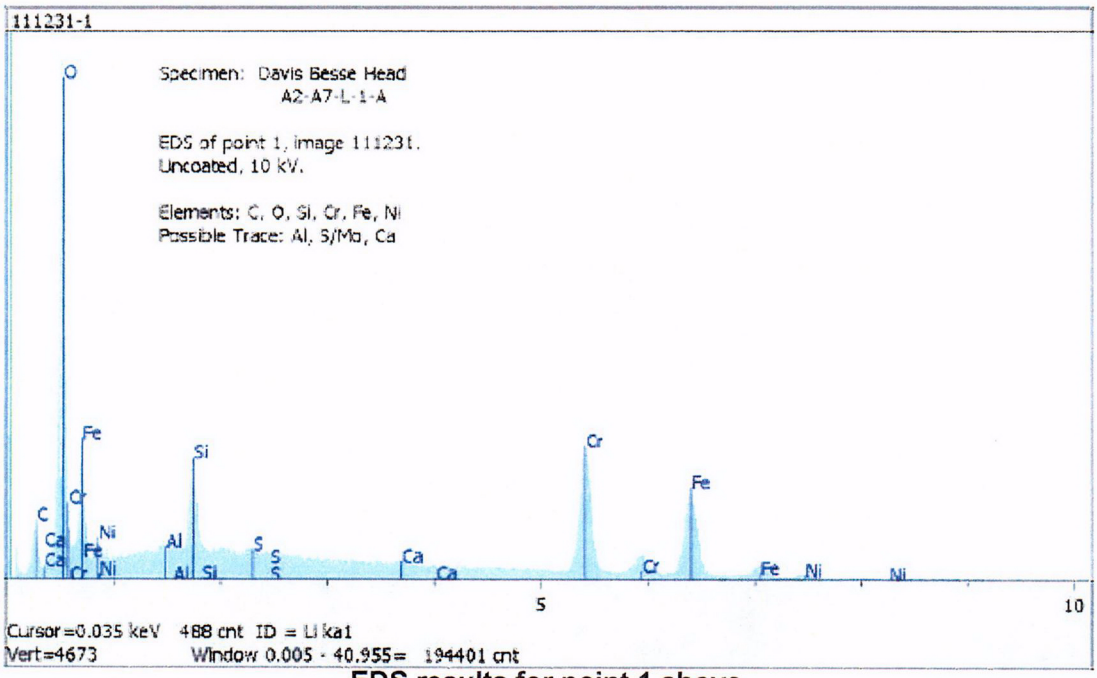

EDS results for point 1 above.

Figure 6.4.1.8: Higher magnification SE micrograph and EDS results for a grain boundary deposit near area "E". This area contained primarily carbon, oxygen, silicon, chromium, iron, and nickel. Lesser amounts of aluminum, sulfur, and calcium were also detected.

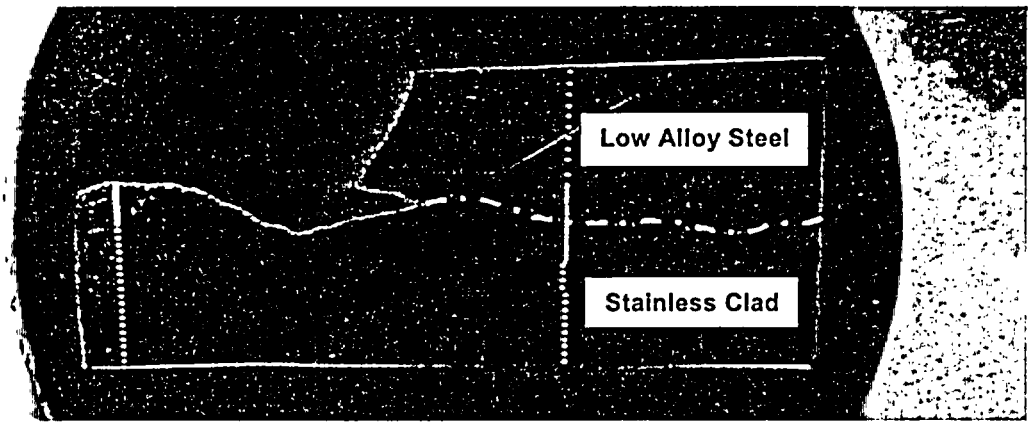

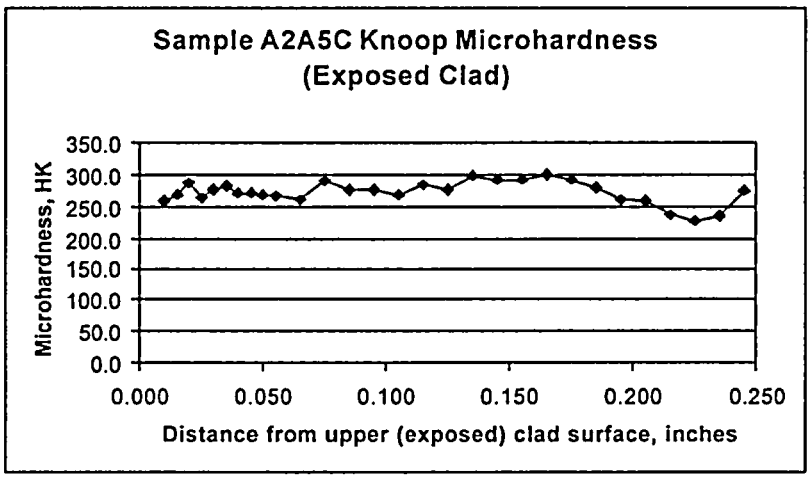

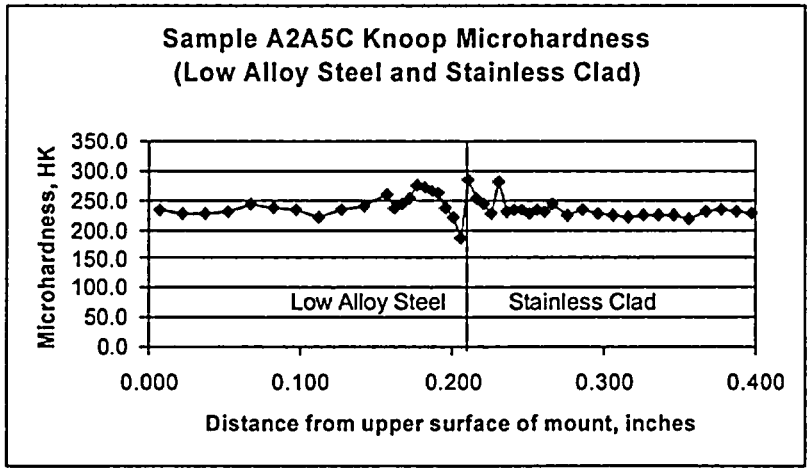

Figure 6.5.1.1: 4X macro photograph of metallographic mount A2A5C, along with Knoop microhardness data. Refer to Figure 5.13 for the sample orientation. The two Knoop microhardness traverse lines are visible in the macro photo. The significant microhardness variations occur in the heat affected zone of the low alloy steel and the cladding adjacent to the fusion line.

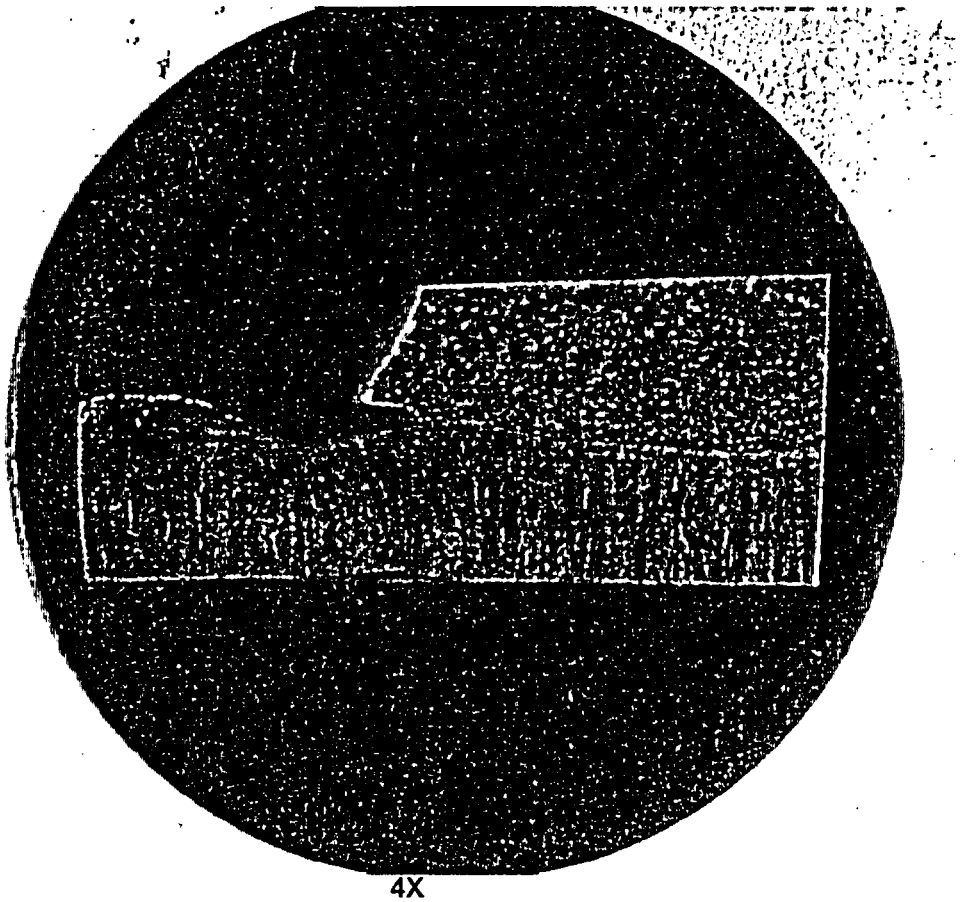

4X

Figure 6.5.1.2: Low magnification photograph of mounted sample A2A5C after chemical etching to reveal the cladding microstructure. It did not appear that a weld deposition change occurred in this region.

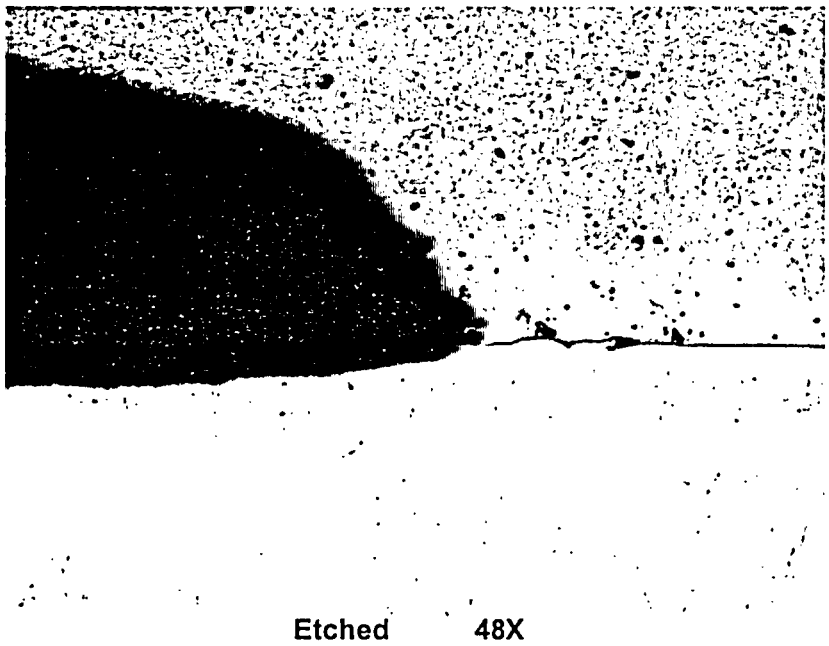

Figure 6.5.1.3: Micrograph showing the undercutting due to boric acid corrosion in the RV head low alloy steel at the interface between low alloy steel (above the notch) and stainless steel cladding (below the notch).

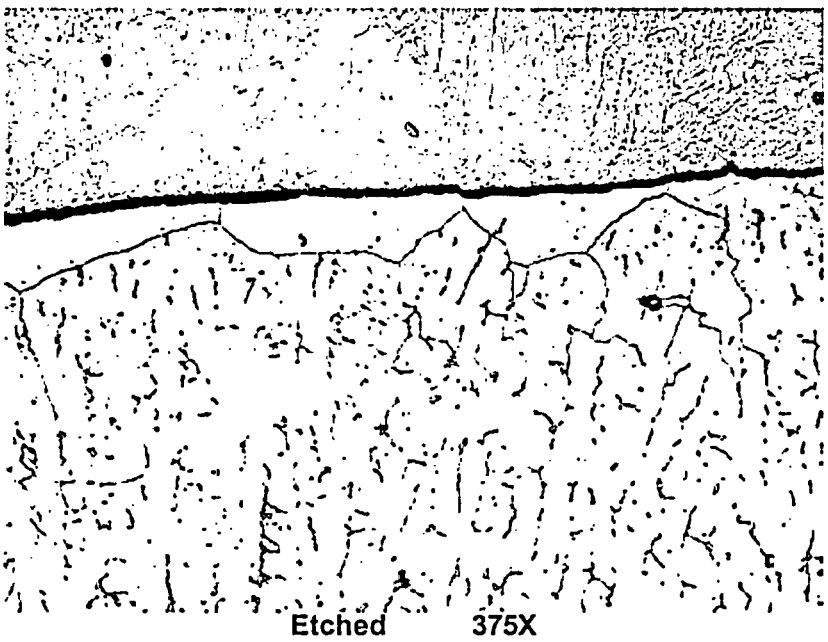

Figure 6.5.1.4: Micrograph showing the interface between low alloy steel (above) and stainless steel cladding (below). The austenitic grains in the first interface layer on the stainless steel cladding side are equiaxed and growing preferentially from the ferrite grains (low alloy steel). The subsequent grain growth in the cladding is columnar.

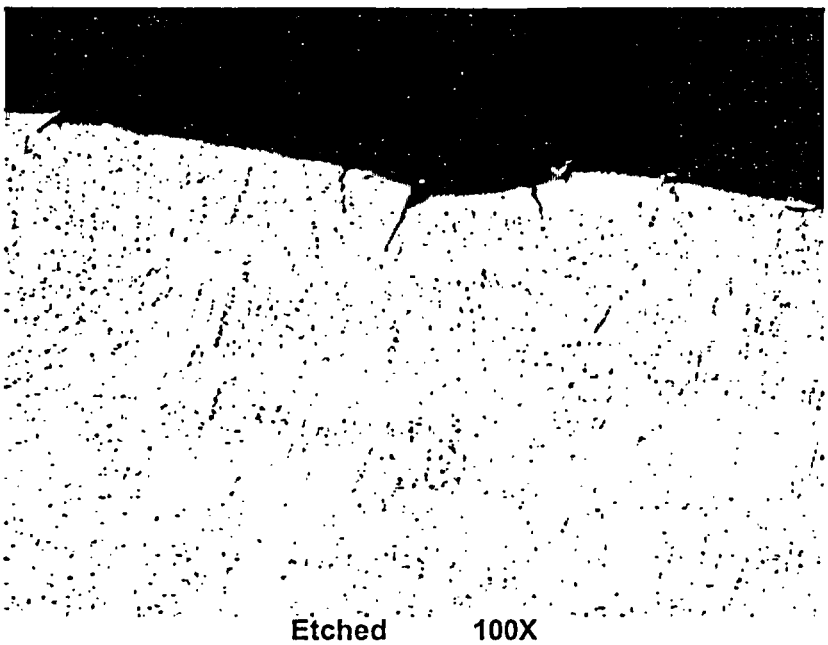

Etched 100X

Etched 375X

Figure 6.5.1.5: Micrographs of the cladding surface exposed due to boric acid corrosion of the RV head low alloy steel. Intergranular attack (IGA) of stainless steel cladding to a depth of the first or second layers of grains is clearly visible. The IGA is probably due to oxygenated and highly concentrated boric acid. There was no evidence of plastic deformation observed in the cladding in this area.

100X

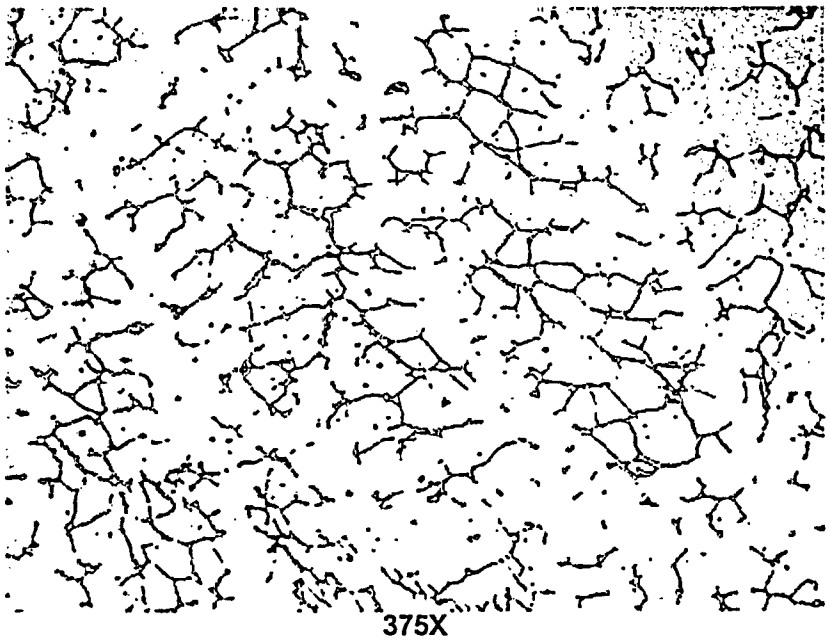

375X

Figure 6.5.1.6: Micrographs showing typical stainless steel cladding microstructure. The dendritic solidification structure is delineated by small pools (or islands) of ferrite in an austenitic matrix.

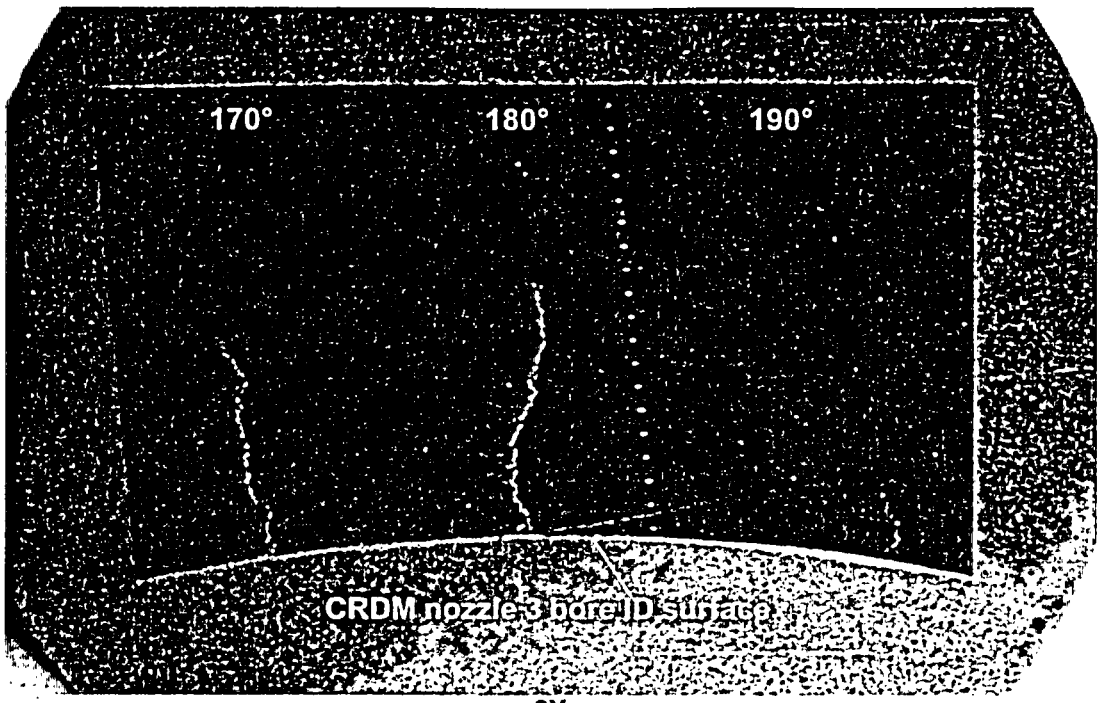

6X

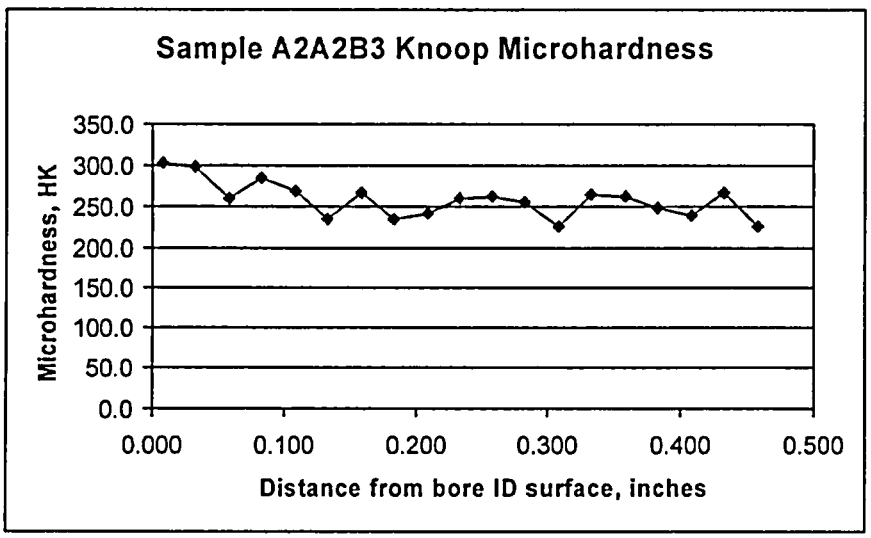

Figure 7.1.1.1: Macro photograph and Knoop microhardness results for metallographic sample A2A2B3 (see Figure 5.2 for the sample orientation). The lower concave surface is the I.D. of the nozzle 3 bore from the nozzle removal process. The crack tips of the two cracks are estimated to be approximately 0.24" and 0.20" below the surface, respectively. The indentations from the microhardness traverse are visible. The elevated microhardness level near the surface is due to the surface cold work layer from the boring of nozzle 3 removal process (see Figures 5.2 and 7.1.1.5).

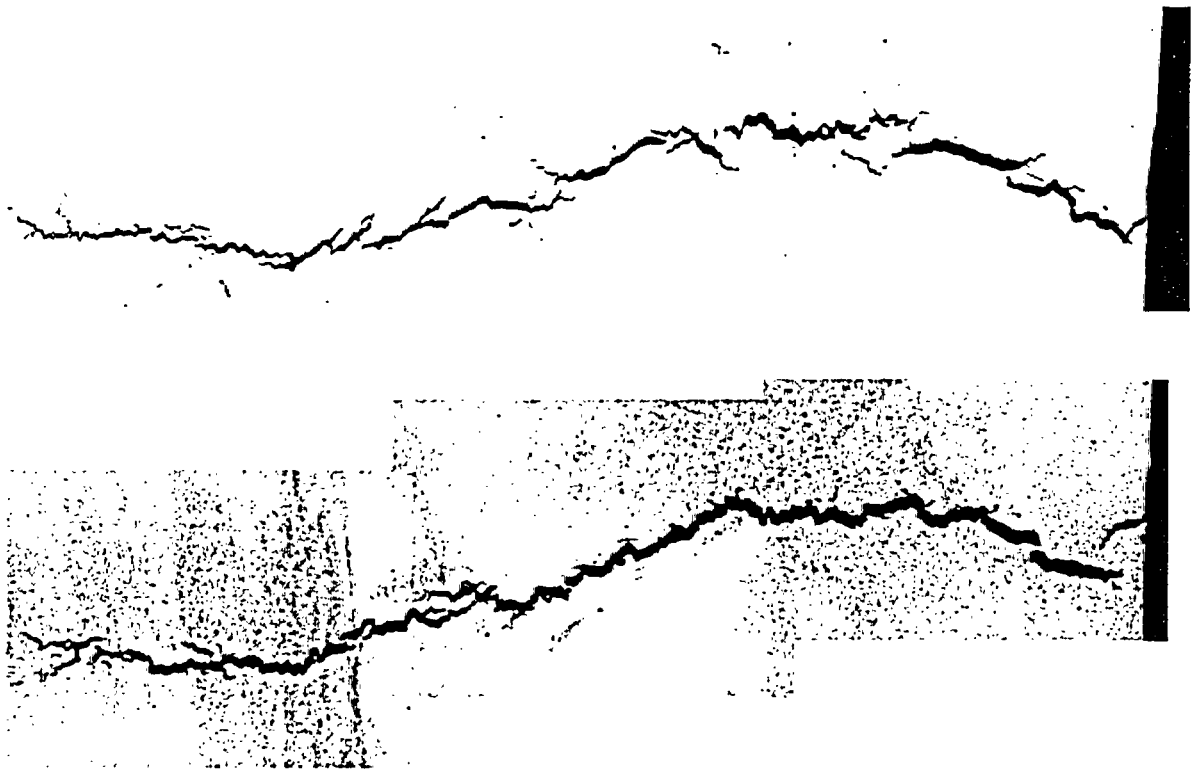

Figure 7.1.1.2: Micrographs showing the crack at ~180° in sample A2A2B3. Top as-polished, bottom etched. Both micrographs 24X.

Etched 375X

Figure 7.1.1.3: Typical microstructure of sample A2A2B3. The grain size and dendritic structure within each grain are consistent with typical Alloy 182 weld.

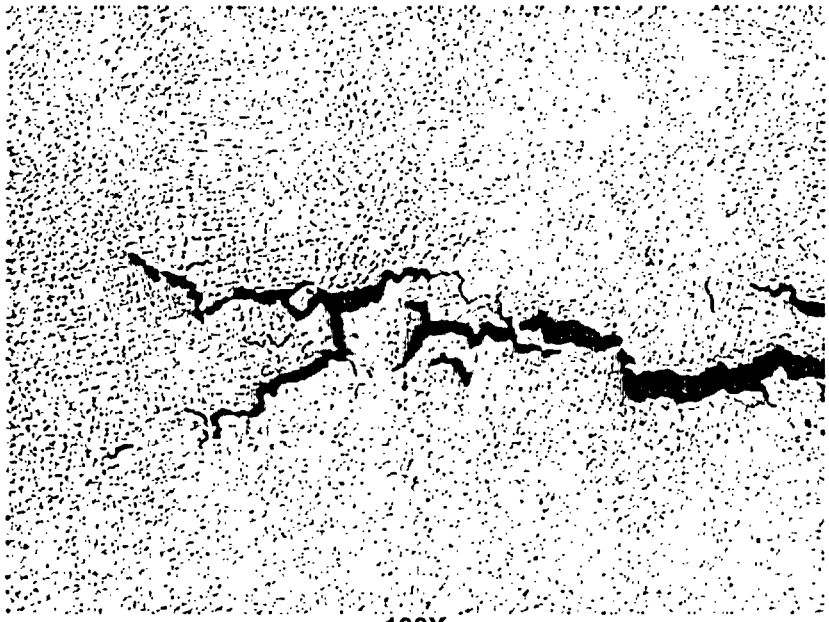

100X

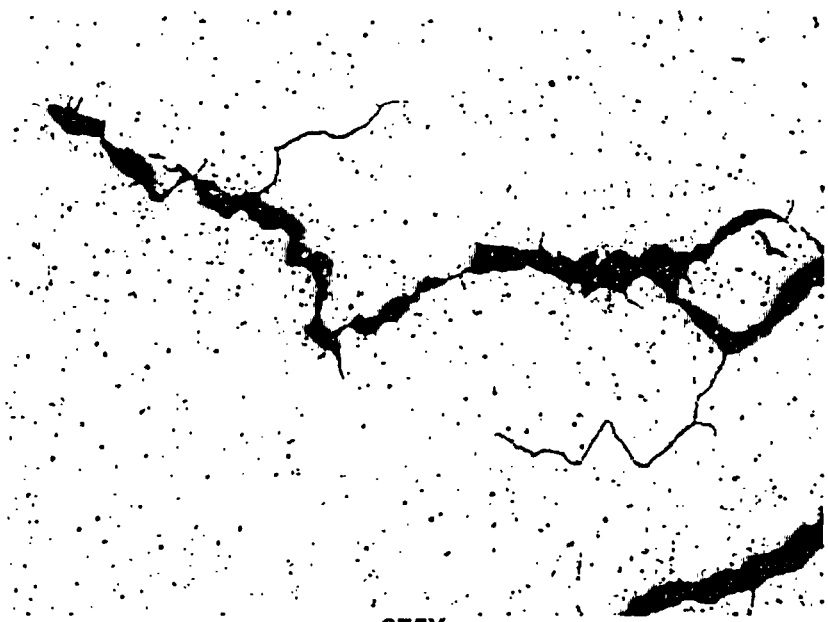

375X

Figure 7.1.1.4: Higher magnification micrographs of the crack tips. Cracking is intergranular or interdendritic.

100X

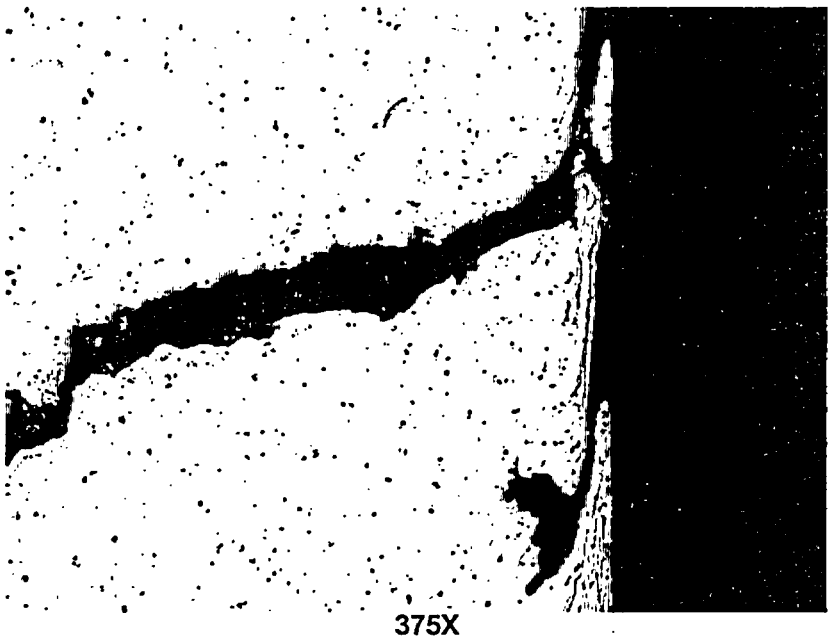

375X

Figure 7.1.1.5: Higher magnification micrographs of the cracking at ~180° near the bored surface. The bored surface shows evidence of surface cold work. The surface cold work is due to the nozzle removal from the RV head and is not related to the J-groove weld fabrication process.

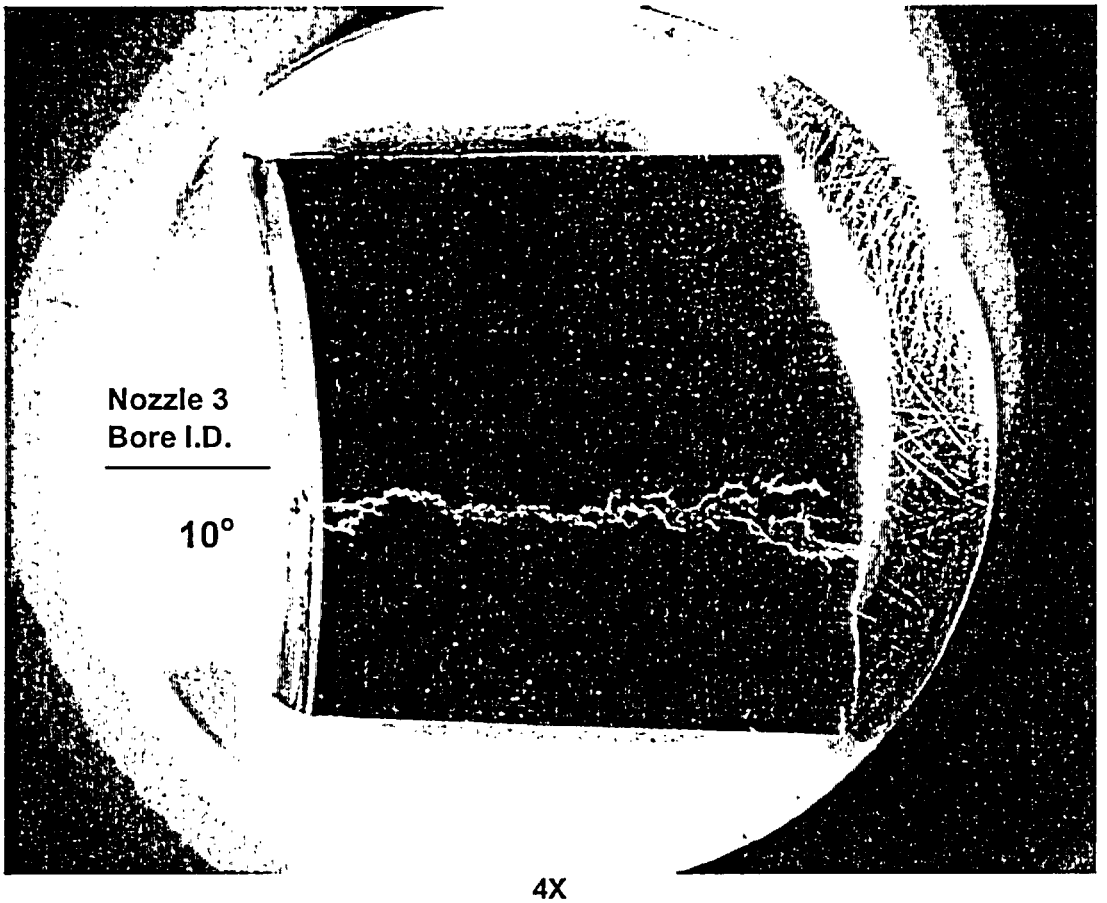

4X

Etched 8X

Figure 7.2.1.1: Macro photograph of metallographic mount sample A2A6B2 (see Figures 5.4 and 5.5 for the sample orientation). The axial cracking at ~10° is through the J-groove weld, in contrast to the cracking near 180°, which was partially through the weld. A slightly higher magnification micrograph is also provided.

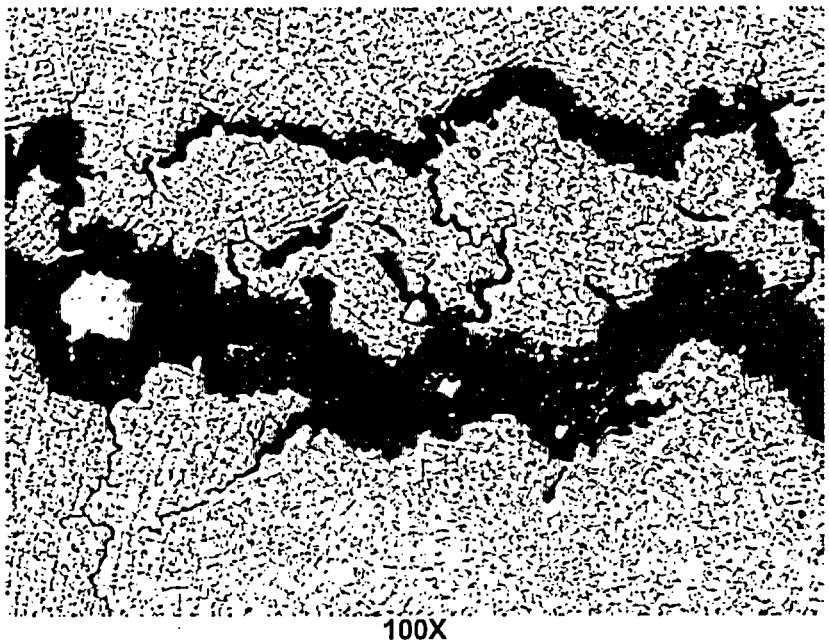

100X

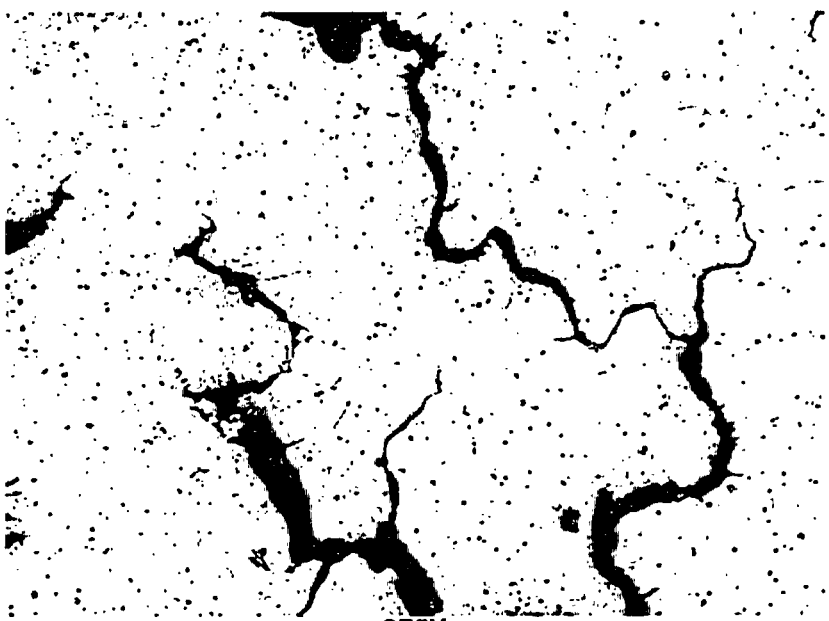

375X

Figure 7.2.1.2: Higher magnification micrographs of the J-groove weld cracking. Cracking is intergranular or interdendritic, similar to the cracking at ~180° in Figure 7.1.1.4.

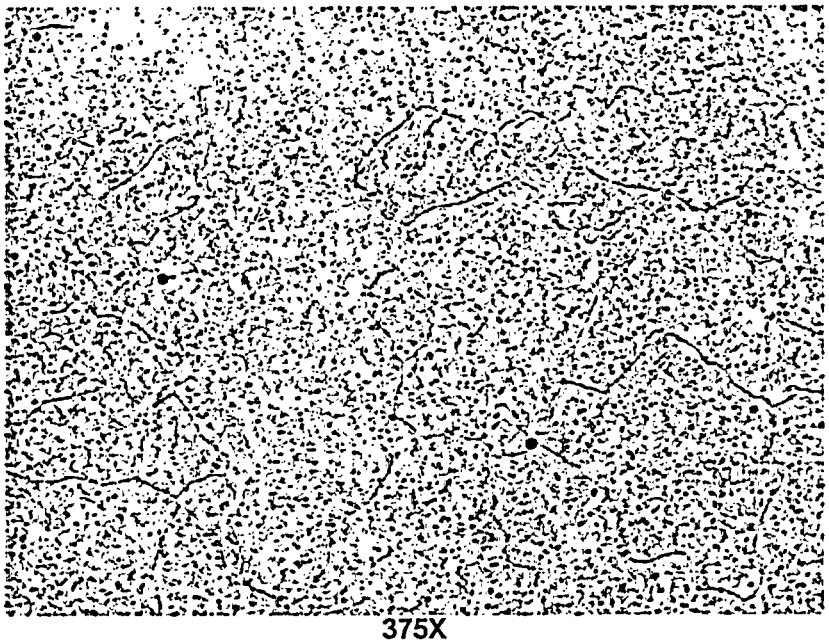

375X

Figure 7.2.1.3: Typical microstructure of sample A2A6B2, which was similar to Figure 7.1.1.3 (at ~180°).

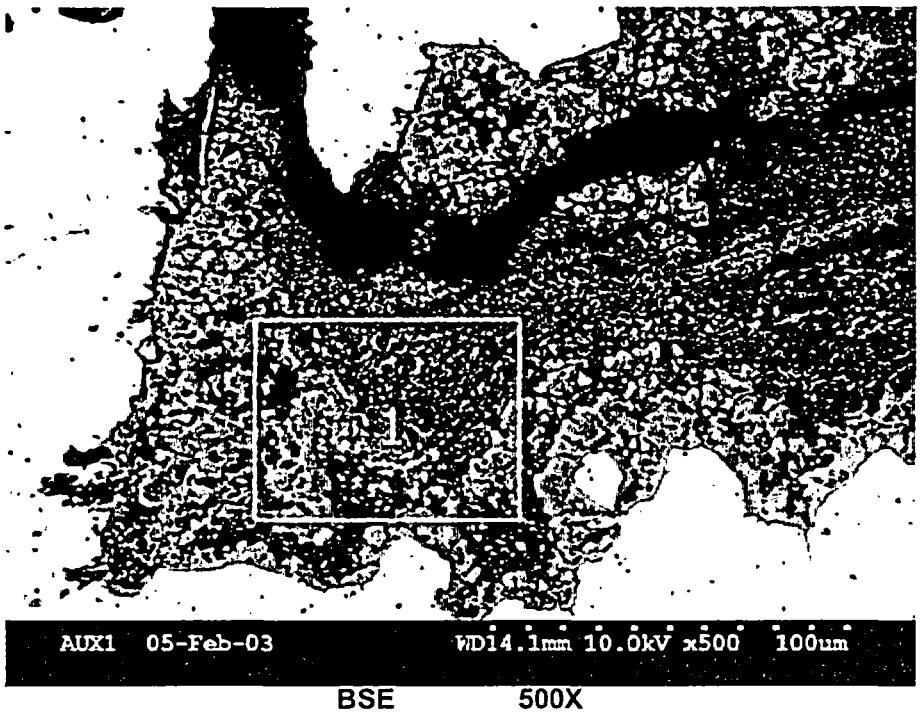

BSE 500X

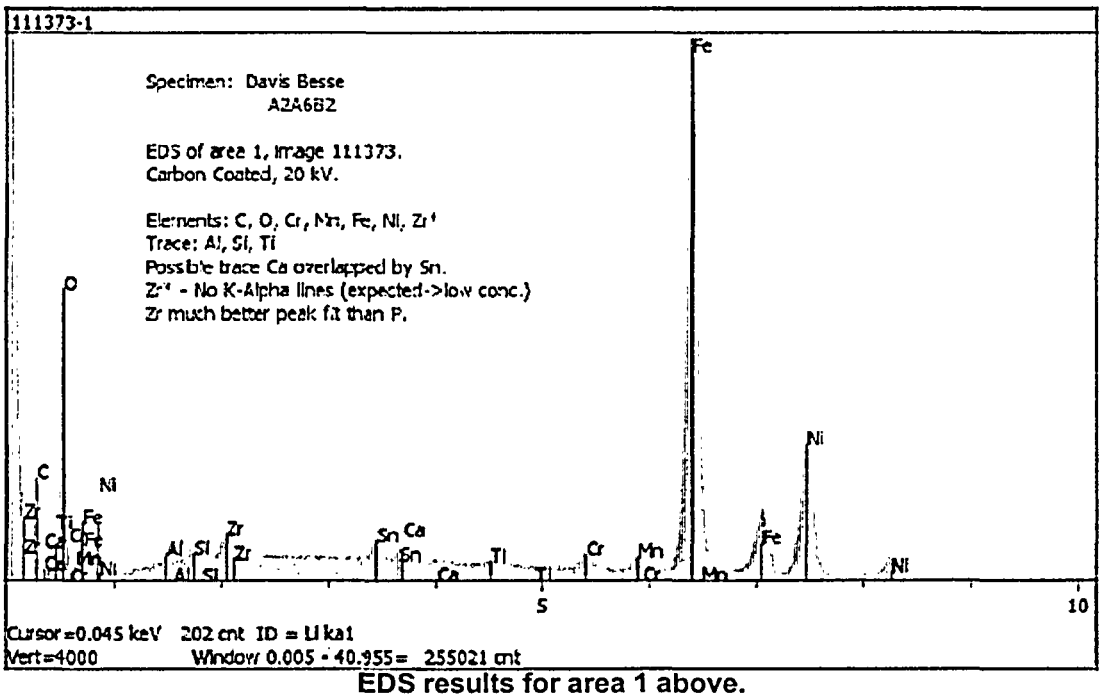

EDS results for area 1 above.

Figure 7.2.2.1: BSE micrograph showing portion of crack filled with corrosion products. The EDS results indicated high concentrations of carbon, oxygen, iron, and nickel.

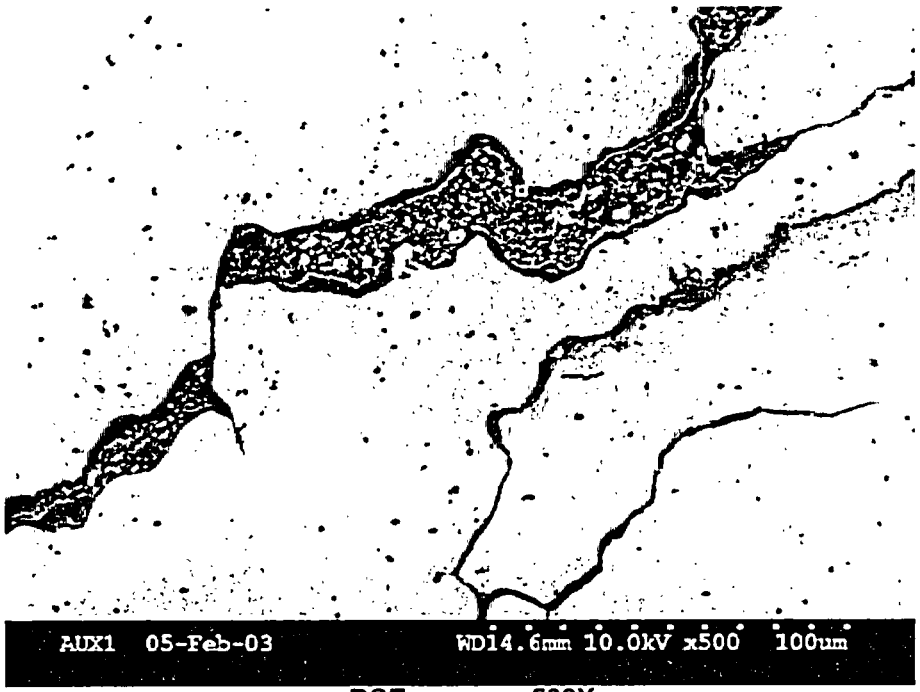

BSE 500X

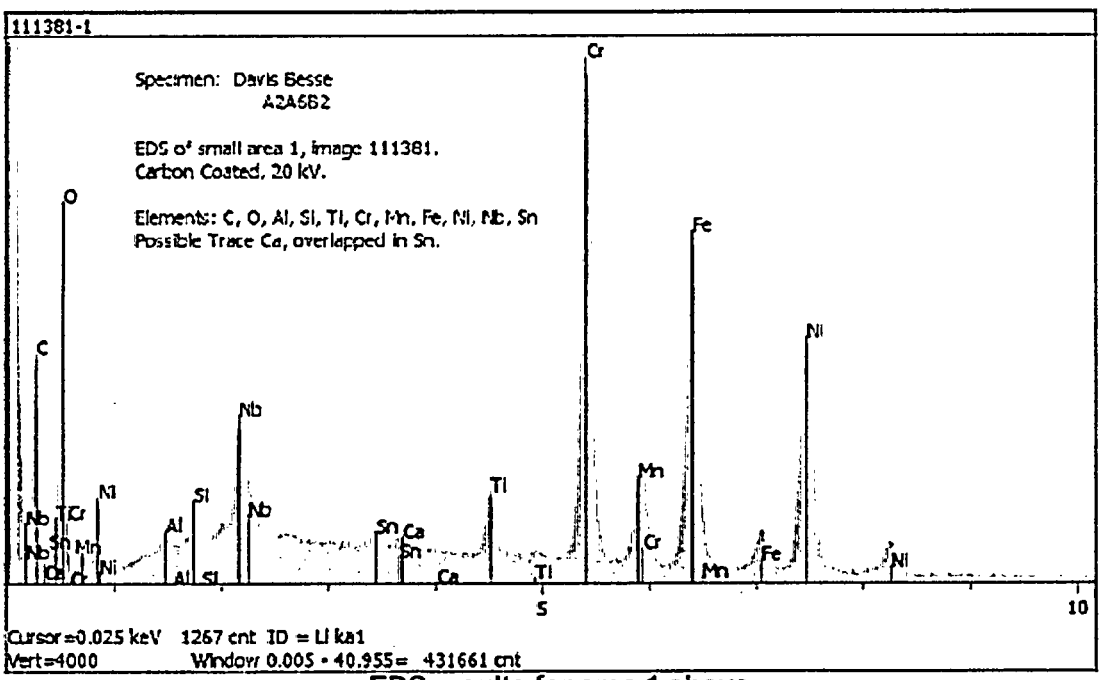

EDS results for area 1 above.

Figure 7.2.2.2: BSE micrograph showing corrosion products near crack tip. The EDS results collected from the area 1 indicated high concentrations of carbon, oxygen, niobium, titanium, chromium, manganese, iron, and nickel.

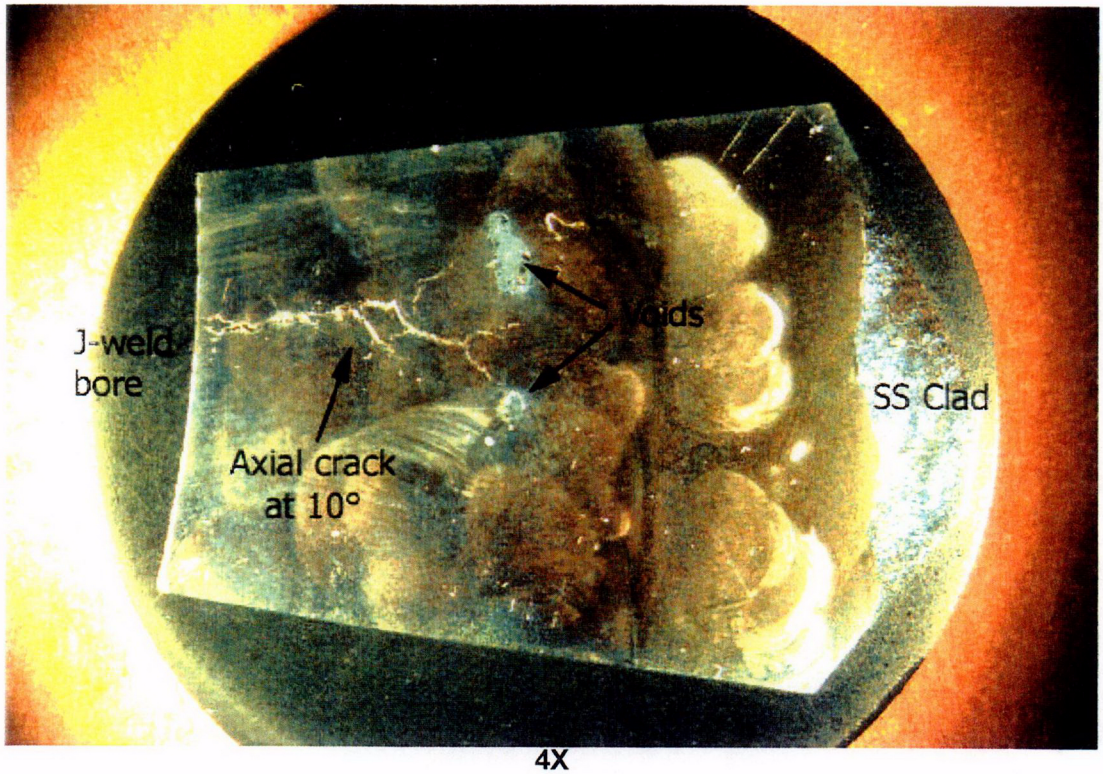

4X

Figure 7.2.3.1: Macro photograph of metallographic mount A2A6A2E1 (see Figure 5.6 and 5.10 for the sample orientation). Cracking was partially through the J-groove weld in the sample plane.

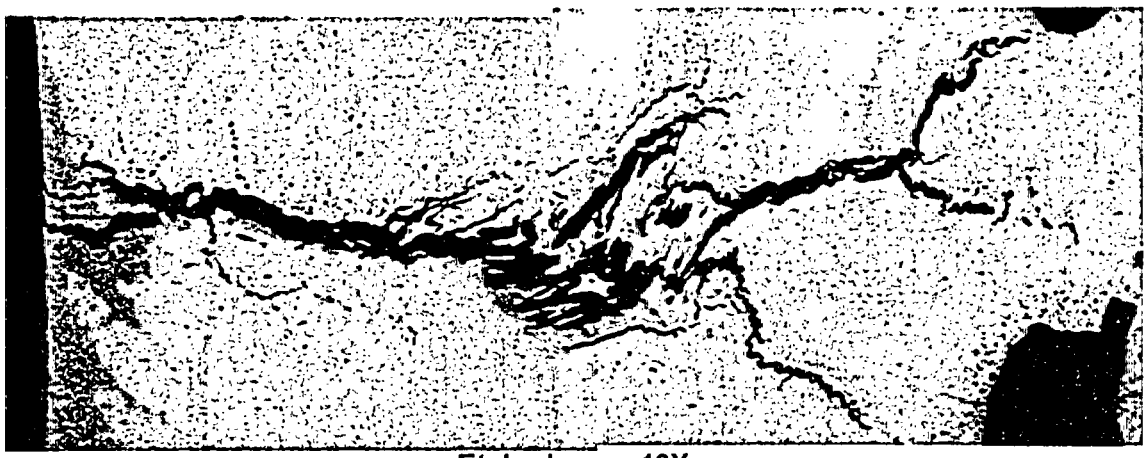

Etched 13X

Figure 7.2.3.2: Micrograph showing axial cracks in the lower portion of the J-groove weld at ~10°. The crack maximum depth is approximately 0.45" beneath the bore I.D. surface.

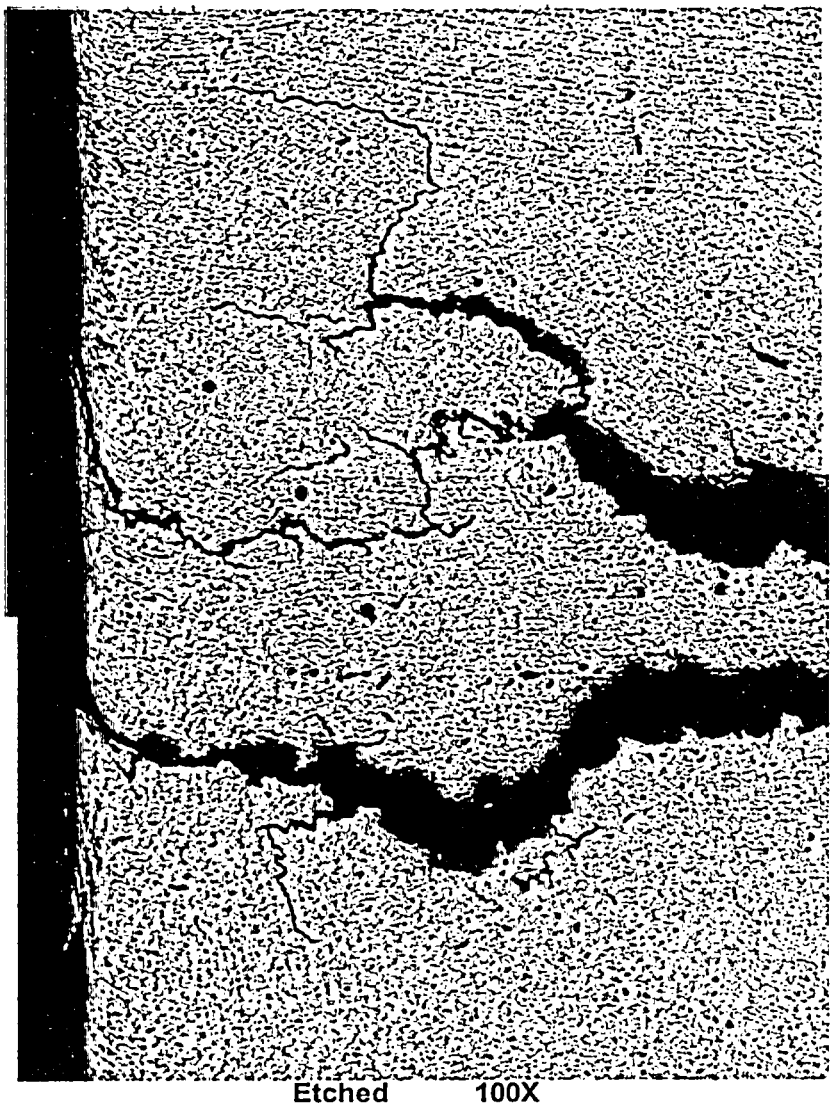

Etched 100X

Figure 7.2.3.3: Cracks located near the bored surface. Surface cold work layer is due to the boring (nozzle removal) process.

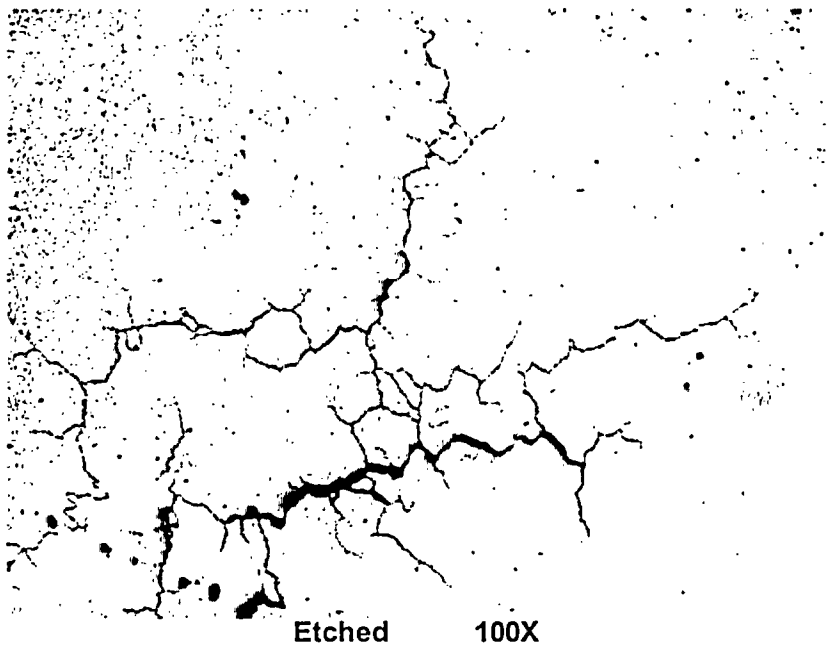

Etched 100X

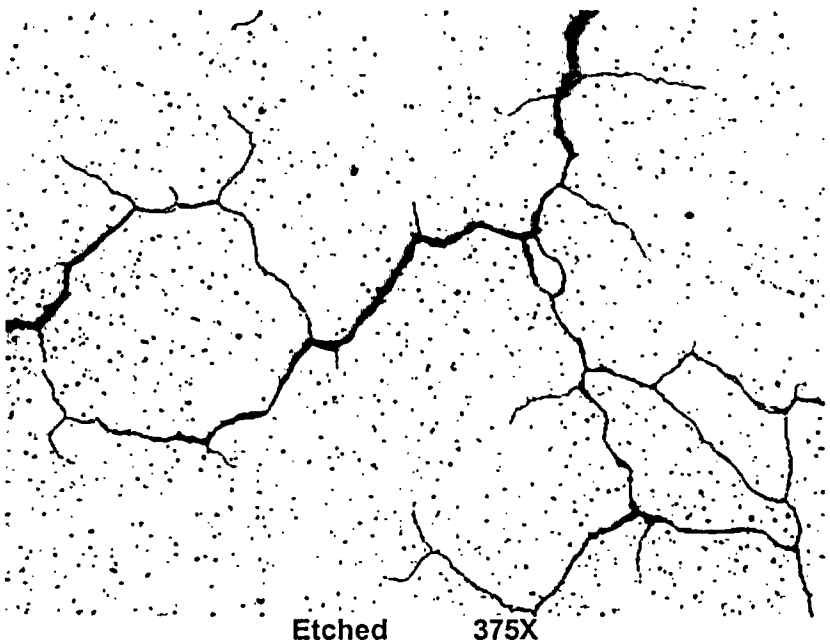

Etched 375X

Figure 7.2.3.4: Interdendritic or intergranular cracking in the J-groove weld away from the bore I.D. surface.

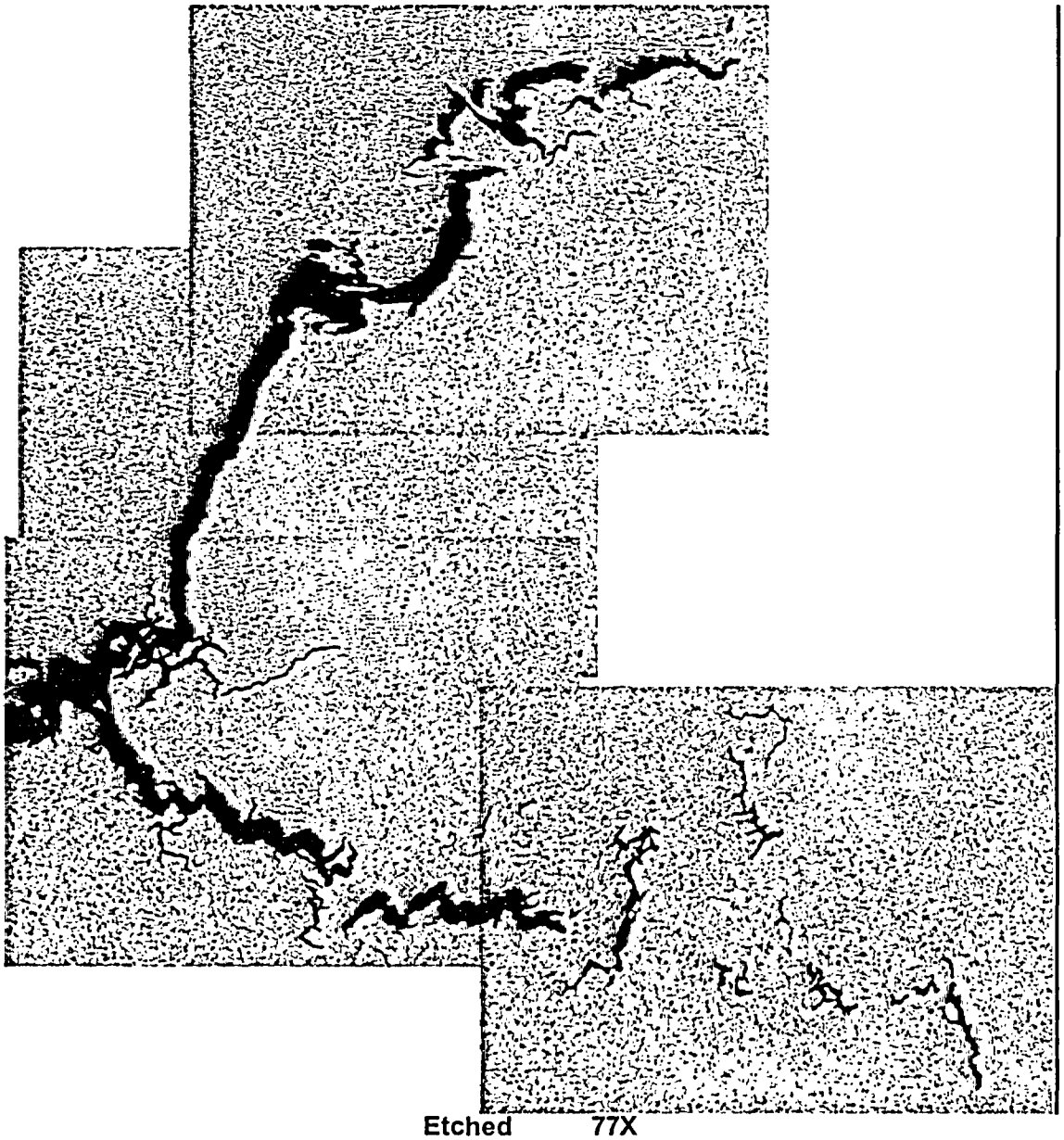

Etched 77X

Figure 7.2.3.5: Crack tips toward the J-groove weld O.D.

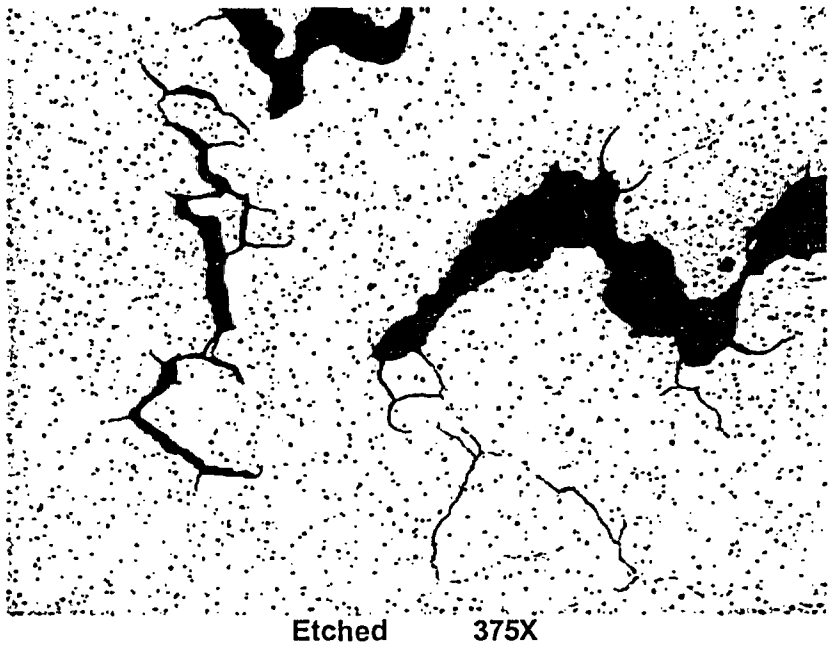

Etched 375X

Figure 7.2.3.6: Crack detail from Figure 7.2.3.5.

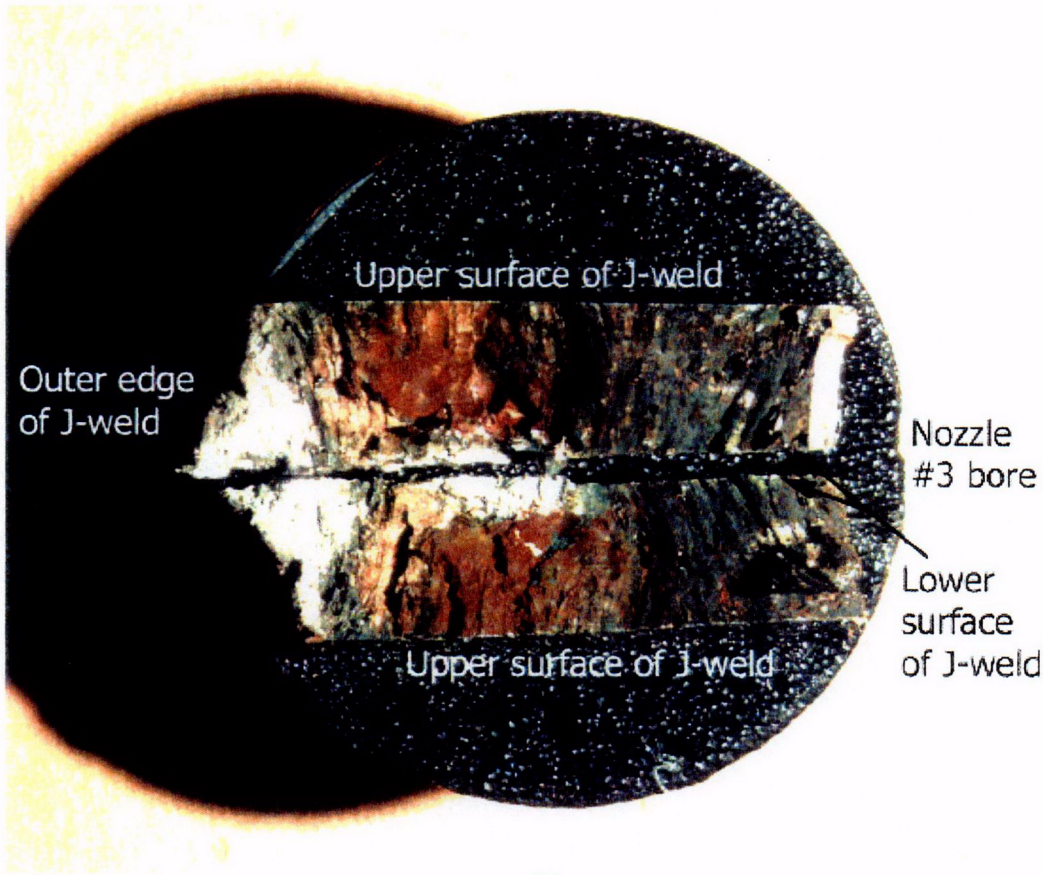

4X

Figure 7.2.4.1: Macro photograph of sample A2A6B3 with the middle portion of the axial cracking at ~10° opened-up for SEM. Refer to Figures 5.4 and 5.5 for the sample location.

C60